UNIVERSIDADE DA BEIRA INTERIOR
Engenharia

Structural Analysis of a Variable-span Wing-box

Rui Filipe Martins Fernandes Cunha

Dissertação para obtenção do Grau de Mestre em

Engenharia Aeronáutica

(Ciclo de Estudos Integrado)

Orientador: Prof. Doutor Pedro Gamboa

Covilhã, Outubro de 2014

To my family and friends

For all their support

Acknowledgements

This work has been partially funded by the European Union's Seventh Framework Programme (FP7) under the Grant Agreement 314139. The CHANGE project (Combined morphing assessment software using flight envelope data and mission based morphing prototype wing development) is a Level 1 project involving 9 partners.

I extend my sincere thanks to all those who, through various forms, accompanied me throughout the preparation of this dissertation. The support I received at the personal and scientific levels, were crucial to this achievement. Without intending to inadvertently forget someone, I must specifically thank some of the most offered significant contributions to this project.

To my family, especially my parents, my brother, grandparents and uncles, I appreciate the support they have given me to accomplish this dream. I hope one day I can return all the effort and confidence they have in me.

I thank Professor Pedro Gamboa for his availability and opportunity given to work on this innovative topic and the knowledge imparted on various material aspects of this dissertation.

I thank Pedro Santos his understanding and the immense help throughout the time I worked with him. Besides the amount of knowledge conveyed, influenced me to take more interest in the topic of this dissertation.

I thank all partners in the CHANGE Project.

I appreciate the patience and generosity of those who contributed to the process of text and formatting dissertation's review, identifying linguistic lapses and rectifying some of its content.

I appreciate every moment I spent with my friends and the mutual help that contributed to the success of all of us.

Last but not least I thank the families Flores da Silva, Mendes and Almeida the encourage words that they told me to continue to struggle to getting through the hard times.

Resumo

Esta dissertação de mestrado descreve o trabalho realizado para analisar a estrutura da caixa de torção de uma asa de envergadura variável. Com base no trabalho realizado anteriormente no projeto CHANGE o principal objetivo desta dissertação é a validação do modelo numérico, feito por Pedro Santos, da caixa de torção envolvente no desenho preliminar para este projeto. Primeiramente foi dimensionado o estaleiro para validar estaticamente este modelo estrutural em que se constituiu o seguinte trabalho. Através do uso de ferramentas computacionais de desenho (CAD) e cálculo numérico, foi projetada e construída a montagem experimental. Com base em ferramentas de análise estrutural computacional, o modelo numérico permitiu o estudo paramétrico, um dos objetivos deste trabalho. De modo a complementar este estudo, foram analisadas várias configurações da asa preliminar para compreender a variação do peso da estrutura e da flexão de acordo com a fração da envergadura móvel. Com a ajuda de ferramentas de programação obtiveram-se dois polinómios calculados a partir das respetivas variações anteriormente descritas. Finalmente foram feitos testes experimentais no protótipo do desenho da asa preliminar.

Palavras-chave

Análise Estrutural; Caixa de Torção; Estudo paramétrico; Modelo Numérico; *Morphing*; Projeto CHANGE; UAV; Validação.

Abstract

This dissertation describes the work done to analyse the wing-box of a variable-span wing. Based on previous work in the CHANGE project the main objective of this study is the experimental analysis of the wing-box structure's prototype build at Universidade da Beira Interior, one of the CHANGE project partners. Surrounding the preliminary design of this project, a numerical model written, concerning a parallel work, was modified and used to analyse the mass and displacement variations according to the moving fraction and semi-span of the morphing wing-box. It was first dimensioned the jig to statically validate this structural model that concerns the following work. Through the use of Computer Aided Design tools and numerical calculation, it was designed and built an experimental setup. Based on computational structural analysis tools, the numerical model allowed the parametric study of the preliminary wing-box design comprising the mass and displacement changes in accordance of the two following parameters: moving fraction and semi-span. In order to complement this study, various configurations of the preliminary wing-box were analysed such as the reduction of the composite sandwich skin's thickness. With the help of programming tools two polynomial functions were calculated from the respective variations previous described. Finally, experimental tests were performed on the prototype of the preliminary wing design. The numerical model was validated and the values are in good agreement.

Keywords

CHANGE Project; Morphing; Numerical Model; Parametric Study; Structural Analysis; UAV; Validation; Wing-box.

Contents

List of Figures

List of Tables

List of Acronyms

ARA	Aircraft Research Association
CAD	Computer Aided Design
CAM	Computer Aided Manufacturing
CFD	Computational Fluid Dynamics
CHANGE	Combined morphing assessment software using flight envelope data and mission based morphing prototype wing development
DARPA	Defence Advanced Research Projects Agency
DC	Direct Current
DLR	Deutsches Zentrum fur Luft und Raumfahrt
EASA	European Aviation Safety Agency
FC	Failure Criteria
FE	Finite Element
FEM	Finite Element Method
IFW	Inboard Fixed Wing
LE	Leading Edge
MALE UAV	Medium Altitude Long Endurance Unmanned Aerial Vehicle
OMW	Outboard Moving Wing
PTFE	Polytetrafluoroethylene
PWM	Pulse Width Modulation
PZT	Piezoelectric
RC	Remote Control
SMA	Shape Memory Alloys
TE	Trailing Edge
THUNDER	Thin Layer Composite-Unimorph Ferroelectric Driver and Sensor
UAV	Unmanned Aerial Vehicle
UBI	Universidade da Beira Interior
UV	Ultraviolet
VAST AUAV	Variable Airspeed Telescoping Additive Unmanned Air Vehicle

Nomenclature

C_L	Wing Lift Coefficient
g	Acceleration due to Gravity, m/s^2
C_l	Aerofoil Lift Coefficient
C_m	Aerofoil Pitching Moment Coefficient
V	Aircraft Equivalent Speed, m/s
α	Angle of Attack, °
V_C	Cruise Speed, m/s
ρ	Density of air, kg/m^3
V_D	Design Dive Speed, m/s
V_B	Design Speed for Maximum Gust Intensity, m/s
δ	Displacement, m
D	Drag, N
L	Lift, N
L/D	Lift to Drag Ratio
n	Load Factor
m	Mass, kg
p	Moving Fraction
M	Pitching Moment, Nm
b	Span, m
V_S	Stall Speed, m/s
θ	Torsion, Nm
S	Wing Area, m^2
C_D	Wing Drag Coefficient
$C_{L\,max}$	Wing Maximum Lift Coefficient
$C_{L\,min}$	Wing Minimum Lift Coefficient

1. Introduction

When we admire the efficiency and elegance of bird flight in Nature, our aviation achievements seem to pale in comparison. Unlike natural fliers, typical aircraft are rigid and inflexible bodies that achieve their design goals through brute force. Inspired by gliding seeds, insects, bats and the flight of birds, work done by researchers in the area of aircraft morphing offers us a chance to achieve some of the efficiency of flight in Nature with aircraft that can operate from space to roads and water. [1]

Designers seek inspiration in order to achieve the simplicity, eleganfice, and efficiency that characterize animal species obtained by thousands of years of biological evolution. [2] Birds are able to manoeuvre in flight with amazing capabilities and aggressive transitions from different flight stages. Avian morphology permits a wide range of wing configurations, each of which may be used for a particular flight task. [3] With the ever-expanding technology in aviation industry, progresses were made in the area of wing design with means of changing the wing or the aerofoil shape in order to expand flight envelopes. Altering the geometry of the wing, known as wing morphing, will lead to an improved performance and/or efficiency over the entire flight of the vehicle. However, in the aeronautical field, there is neither an exact definition nor an agreement between the researchers about the type of geometrical changes necessary to qualify an aircraft as shape morphing. Morphing is short for metamorphose and is adopted to define "*a set of technologies that increase a vehicle's performance by manipulating certain characteristics to better match the vehicle state to the environment and task at hand*". [4]

The deployment of conventional flaps or slats on a commercial airplane changes the geometry of its wings that allows the aircraft to fly at a range of flight conditions, but the performance at each condition is often sub-optimal. Moreover, these geometry changes are limited, with narrow benefits compared with those that can be achieved from an adaptable wing. Although significant geometry changes of an aircraft wing during flight may allow an approach to the optimal performance, multi-role missions are not possible with a fixed-geometry aircraft.

Morphing aircraft are capable of the best performance at all flight stages. This can be achieved by means of crowding different concepts and configurations. So, in-flight change of aerofoil or wing's characteristics became the most sought solutions for morphing.

1.1. Motivation

Ever since the dawn of aviation, wing morphing has been used for aircraft control. In 1903, the Wright Brothers were the first successful aviators to use wing warping in an actual flight test which enabled roll control by changing the twist of its wing using cables actuated directly by the pilot. [5] Most all of the Wrights' predecessors who studied flight were concerned with constructing naturally stable aircraft and therefore control was less of an issue.

In the 1990s aircraft morphing focused mainly on improving the efficiency of wing and control surfaces. In the twenty-first century work continues on improving flight efficiency, but advances in lightweight and smart materials, efficient innovative actuators and control systems have pushed the research and development focus to expanding the range of operational environments. This performance enhancement capability was demonstrated in Tidwell's *et. al.* [6] work, where the Firebee drone base design was subjected to both aerofoil and planform optimization for each flight stage and manoeuvres. The positive results on the two optimization designs in comparison to the base design are plotted in Figure 1.1. The need for innovation allowed to increase energy efficiency by means of less power required and, therefore, fuel consumption reduction.

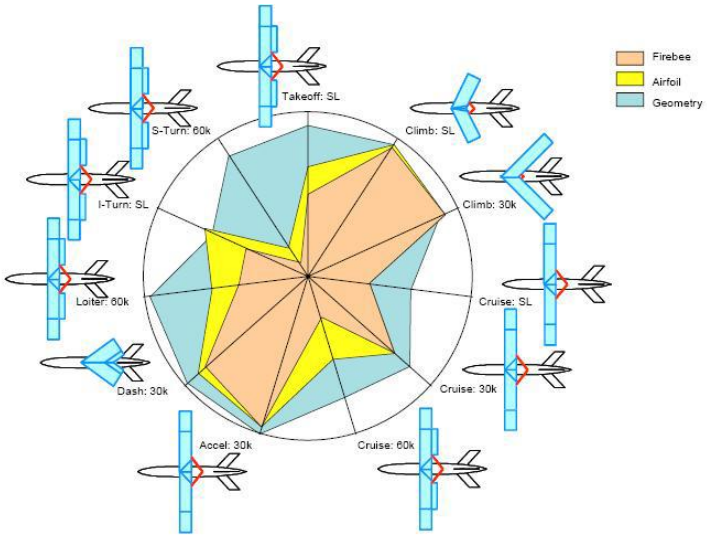

Figure 1.1: Spider plot comparing performance of the base-design Firebee, the morphing aerofoil Firebee and the morphing planform Firebee [6]

Furthermore, in recent years, focus has moved to small aircraft, unmanned aerial vehicles, or UAVs. The move toward UAVs results from greater efficiency requirements, low cost on production and operation, and a short time-to-deliver because of reduced certification issues and qualification tests. The lower aerodynamic load on UAVs also increases the number of potential morphing technologies. NextGen also studied the potential benefit of wing morphing. The results in terms of system-level performance improvements are illustrated in the spider plot in Figure 1.2, in which we can see the flight performances shown for fixed and morphing wings. The outmost points represent the theoretically best performance at each of the designated flight conditions. [7]

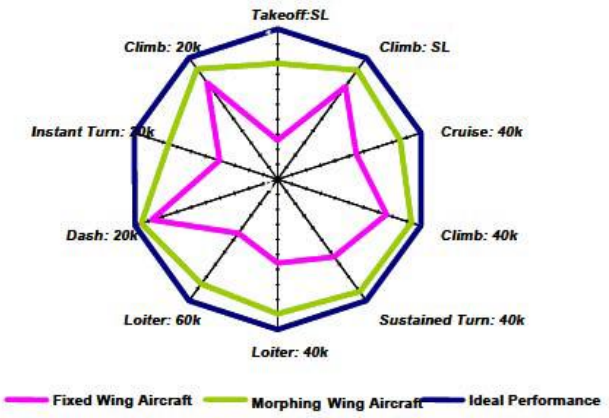

Figure 1.2: Spider plot comparison of NextGen's fixed and morphing wings aircraft [7]

The timeline in Appendix A.1 highlights that most large shape modification techniques have been developed for military applications, where a more versatile vehicle compensates for the additional complexity and weight.

The reason behind the investment made on morphing research is concerned with the technology that exists today. New, novel materials, material systems, and actuation devices have been developed during the past decade. These developments allow designers to distribute actuation forces and power optimally and more efficiently. Properly used, these devices reduce weight compared to other, more established designs.

1.2. Benefits and challenges

The current use of flaps and slats represents a simplification of the general idea of morphing. Traditional control systems give high aerodynamic performance over a fixed range or limited set of flight conditions. Outside this range, these systems can have a negative influence on the aerodynamics and give lower efficiency. Conventional hinged mechanisms are effective in controlling airflow but they are not efficient as the hinges and other junctions create discontinuities in the surface, resulting in unwanted fluid dynamic phenomena.

The use of UAVs as a test platform for wing morphing technology can be attributed to their complex flight mission profiles, as well as their requirement to dynamically change their mission profiles during flight. For comparison, a commercial airliner can spend 90% or more of its flight mission cruising. As a result, their fixed wings are designed to achieve one optimal performance during cruising - highest lift-to-drag ratio. Even if the wings are slightly inefficient during the remainder of the flight mission profile, the overall mission efficiency will not be greatly decreased. Most UAVs have mission profiles that require them to cycle between loitering, cruising, dashing, fast ascents and descents. [8]

As shown in Figure 1.3, each of these stages of the mission profile becomes a bigger component of the overall mission, so it would make sense to try to design a wing which will offer optimal flight performance over the entire mission profile.

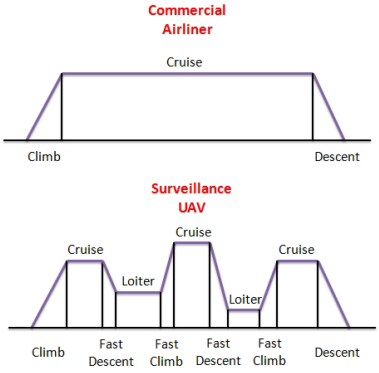

Figure 1.3: Comparison of mission profiles for a generic commercial airliner vs. a generic surveillance UAV [8]

According to Anderson [9], aircraft wing morphing cannot be successfully implemented without addressing several challenges that arise when adding a mechanical morphing mechanism to a structural wing. Costs associated with specific wing morphing changes are also briefly summarized in Table 1.1.

Table 1.1: Characteristics of wing-level morphing [9]

Morphing type	Performance effects	Benefits	Cost
Sweep	Drag divergence and Mach number	Useful for performing dash manoeuvres and high-speed flight	Lower lift Coefficient; higher weight
Cant	Lateral stability	Positive cant increases lateral (roll) stability while negative cant increases manoeuvrability; possibility for instantaneous winglets to reduce induced drag	Increased stability results in decreased manoeuvrability and vice versa
Twits	Lift, drag and moment	Control of aerodynamic forces and moments; ability to maintain level body; useful as high lift and control surface	Lower wing torsional rigidity and moment
Span	Aspect ratio and wing loading	Larger aspect ratio increases performance parameters; shorter span increase manoeuvrability	Large span results in large wing root moments

Kudva *et.al*. [10] stated that the type of improvement sought on a morphing wing is highly dependent on the wing parameter, and no single wing parameter is optimum for every flight characteristic. Thus, different flight conditions call for dramatically different and conflicting wing properties. So, in order to have the same aircraft performing well for different flight conditions, the aircraft should be capable of making large configuration changes in reversible manner. Table 1.2 shows in detail the effect of each wing parameter on aircraft performance.

Table 1.2: Effects of wing geometric parameters on aircraft performance [10]

Parameter		Effect of variability (all other parameters unchanged)
Wing Planform Area	↑ ↓	Increased: Lift, load factor capability Decreased: Parasitic drag
Wing Aspect Ratio	↑ ↓	Increased: L/D, loiter time, cruise distance, turn rates Decreased: Engine requirements Increased: Maximum speed Decreased: Parasitic drag
Wing Dihedral	↑ ↓	Increased: Rolling moment capability, lateral stability Decreased: Maximum speed
Wing Sweep	↑ ↓	Increased: Critical Mach number, dihedral effect Decreased: High speed drag Increased: Maximum Lift Coefficient
Wing Taper Ratio	-	Wing efficiency (spanwise lift distribution); induced drag
Wing Twist Distribution	-	Prevents tip stall behaviour; spanwise lift distribution
Aerofoil Camber	-	Zero-lift angle of attack, aerofoil efficiency, separation behaviour
Aerofoil Thickness/Chord Ratio	↑ ↓	Improved: low-speed aerofoil performance Improved: High-speed aerofoil performance
Leading Edge Radius	↑ ↓	Improved: Low-speed aerofoil performance Improved: High-speed aerofoil performance
Aerofoil Thickness	-	Aerofoil characteristics, laminar/turbulent transition

From the structural perspective the objective is to produce fully integrated, hierarchical structures with compliance control. The requirements of the structure are conflicting: the structure must be stiff to ensure the external loads cause only small deformations, but must be flexible to enable shape changes. The only solution to this conflict is to carefully design the structure to decouple these two actions. The skin of a morphing aerofoil is a good example. The skin must be stiff to withstand the aerodynamic loading, but flexible to allow the aerofoil section to deform.

One particular challenge is the development and implementation of suitable morphing skins. Different morphing capabilities impose distinct requirements on the skin resulting in motions that are predominantly shearing, bending and torsional, and extension/retraction movements, thus the skin must be able to adequately support all referred motions. Any combination of the former, places additional and more complex requirements on the skin. Regardless of the morphing motion, a morphing skin must maintain the aerodynamic integrity of the wing, distribute pressure and shear force distribution to the supporting structure and avoid imposing additional requirements or constraints on the morphing mechanism.

1.3. Similar work

Passive morphing aerofoils, inflatable wings and morphing rotary wings are briefly described in this chapter although they are not directly related to the current study.

Passive morphing may improve the aerodynamic characteristics through structural shape change by aerodynamic loads during the flight, resulting in improving fuel efficiency. The passive morphing structure should have a capability to be highly deformed while maintaining a sufficient stiffness in bending. Honeycombs may be good for controlling both stiffness and flexibility. Some researchers (such as Bettini *et. al.* [11] and Vos and Barrett [12], e.g.) investigated the static deformations through the fluid-structure interaction using computational fluid dynamics and structural finite element analysis, and also fabricated varying geometry honeycomb prototypes for testing. Experimental results confirm the appealing properties of honeycomb aerofoils.

In 2001, NASA Dryden proved it is feasible to use an in-flight deployment inflatable wing and have since sparked research in the development of using this concept for a morphing UAV wing [13]. Much research has been done in the past years on many aspects of inflatable wings (such as J. M. Rowe *et. al.* [14] and A. Simpson *et. al.* [15], e.g.). Inflatable wings use span-wise inflatable gas baffles or structural cavities that once inflated, use the required constant internal pressure to maintain the wing's shape. Current materials research suggests that a typical skin material used for an inflatable wing is an ultraviolet curing resin that, once exposed to the UV rays, becomes rigid. [14]

Rotary-wing aircraft have challenged aeronautical engineers with plenty of issues to obtain stable flight. A major component of these issues is the complex flow field that a rotor blade is exposed to. Even in hover, each section of the rotor blade has different oncoming flow velocities, and engineers have designed the blade with a pre-built twist angle to compensate for that. However, the optimum amount of this pre-twist angle varies with the flight condition, and hence classical rotor blade designs are a compromise. Current research on rotary wings focuses on improvements in terms of increased speed, payload, and manoeuvrability, along with reductions in costs, vibrations, and noise and so morphing on rotary-wing aircraft is, nowadays, usually seen.

1.4. The CHANGE project

CHANGE (Combined morphing assessment software using flight envelope data and mission based morphing prototype wing development) is a Collaborative Project financed under the Transport (including Aeronautics) theme of the Cooperation Programme of the 7th Framework Programme of the European Commission. The CHANGE project started on the 1st of August 2012, and will have an expected duration of 3 years. A total of 9 partners participate in this project based in 4 different European Member States and 1 European Associate Member State. [16]

The CHANGE project focuses on the development of a suite of assessment tools, ranging from low to high fidelity, suitable for analysis of morphing wing planforms. These tools are used within the project to develop and assess a small/medium UAV platform, designed for loiter reconnaissance, with multiple contemporary morphing concepts integrated into the wing structure. The work proposed includes: development of a low fidelity assessment framework, high fidelity tools to validate low fidelity models and provide analysis and assessment data of the platform, a wing that integrates multiple morphing concepts onto the wing along with supporting wind-tunnel and flight test data.

Objectives of the project include: providing a basis for further research into the synthesis and integration of morphing technologies; highlighting the challenges of analysis and integration of these concepts onto working platforms; development of a tool to enable assessment of a morphing concept using both low and high fidelity modelling methods.

1.4.1. Technical specification

The UAV mission phases are shown in Figure 1.4. The mission starts with the take-off, followed by a levelled high-speed cruise. After some changes in altitude, the UAV must perform a loitering time and the last phase is the landing.

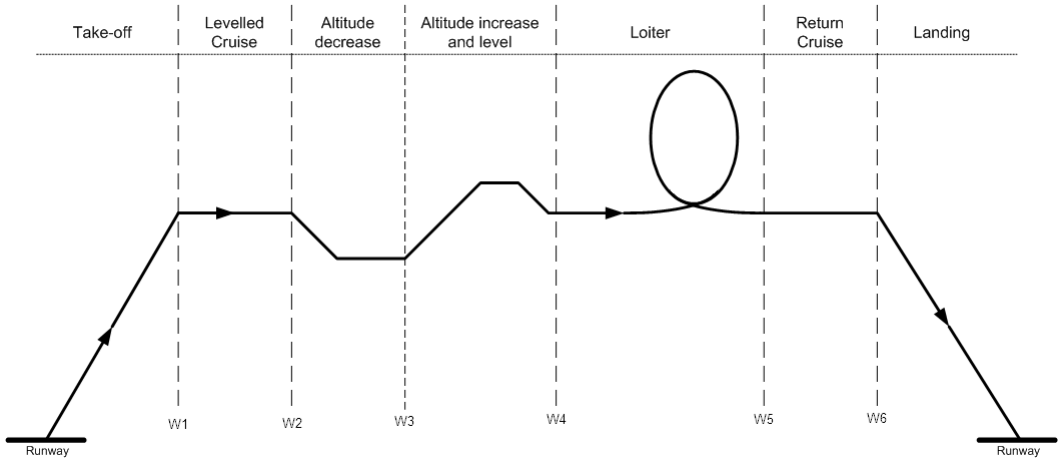

Figure 1.4: Mission in the CHANGE project [16]

The considered morphing technologies and specifications for the wing-box are the wing-span extension, camber morphing and modularity. The later three topics are summarized next:

- **Wing-Span Extension:** wing span can vary from a minimum of 3 m (75% of the maximum wingspan) to a maximum of 4 m. For the semi-span, the latter corresponds to a minimum value of 1.5 m to a maximum value of 2 m;
- **Camber morphing:** Camber morphing is an intentional variation of the camber of the wing section from root to tip. The camber variation is achieved by leading and trailing edge morphing surfaces;

- **Modularity:** The wing-box is the core structure of the wing which will take most of the bending and torsion loads of the wing. The leading edge and trailing edge surfaces will be added to the front and to the rear of the wing-box, respectively, in a manner to be defined but which does not incur in aerodynamic penalties. The mechanisms, including structure, actuators and wiring, required for the telescopic motion are placed inside the wing-box. The mechanisms of the leading edge and trailing edge morphing surfaces are placed inside themselves.

During all flight phases the UAV has a constant mass of 25 kg.

1.5. Scope of current study

The current study has two main objectives which are the following:

Understand how the wing-box's moving fraction and semi-span influences its structure's mass and deflection in three different wing-box configurations (concerning composite sandwich skin's thickness reduction) through a parametric study based on a numerical model written, concerning a parallel work. Surrounding the preliminary design of this project, the numerical model was modified and used to analyse the mass and displacement variations according to moving fractions from 0.05 to 0.3 and semi-spans of 2 m, 2.5 m and 3 m of the morphing wing-box;

Experimental test of the wing-box structure's prototype build at Universidade da Beira Interior taking into account that the specimen tested was according to the preliminary wing-box design. A jig was dimensioned to implement the experimental setup. The wing-box was clamped at its root and was statically tested with two distributed forces to represent the aerodynamic loads used in the numerical model.

1.6. Outline

The first chapter is constituted by the introduction, motivation and the scope of the current study. Also in this chapter the benefits and challenges, similar work, a summary of the CHANGE Project and the outline of the dissertation's content are presented. The following chapter presents the state-of-art of morphing categories and applications as well as some structural analysis papers. In the third chapter, the telescopic wing concept is explained. Chapter four encompasses the parametric study of the wing-box which involves the numerical model's manipulation and theoretical results obtained. The fifth chapter presents the experimental tests and the results obtained. The sixth chapter presents some conclusions drawn out from the current work and suggestions for future work. The seventh and eighth chapters are the references and appendix, respectively.

2. Literature review

As stated earlier, people have been fascinated by flight. The aerospace field as we know it today uses human-developed technology to reach the sky limits. German engineering company Festo[1] has successfully deciphered the wing and body language of how a bird takes flight and embodied those natural principles in the *Smartbird*. [17] Figure 2.1 shows Festo, the *Smartbid* at different stages of flight.

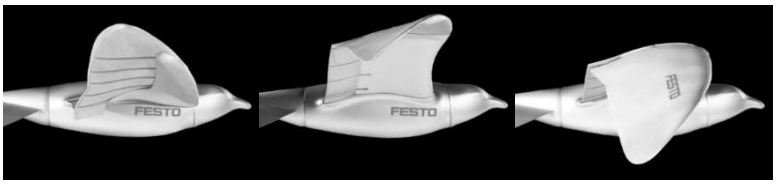

Figure 2.1: Festo, the Smartbird at different stages of flight [17]

Other recent investigations are taking place at NASA. Planetary exploration missions using robots that mimic birds and insects flight could enable unique access to measure phenomena in extreme terrains to accomplish science objectives. Flapping-wing drones (Figure 2.2) are practical vehicles that could be deployed on missions launched from Earth. [18]

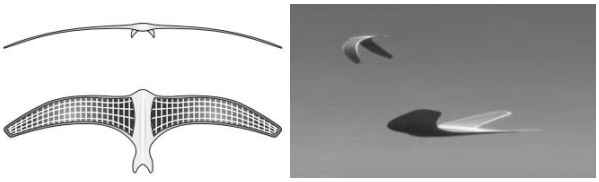

Figure 2.2: Flying mechanism that emulates birds was conceived for planetary exploration missions [18]

As we can witness, nature will always be present in flight. Plants use many methods of dispersing their seeds, including being blown in the wind and being shaped in an aerodynamic configuration to enable the largest distance to be travelled. There are various aerodynamic configurations of seeds, and two examples are shown in Figure 2.3 where the seed of the tree *Tipuana tipu* has a wing that propels it in the wind. It is also interesting to mention the tropical Asian climbing gourd, also in Figure 2.3, *Alsomitra macrocarpa*, a tree with a relatively large seed. [1]

Figure 2.3: Tipuana tipu (at left) and Alsomitra macrocarpa (at right) seeds [1]

[1] Independent company segmented in automation technology and didactic sectors.

Sofla *et. al.* [19] and Barbarino *et. al.* [2] categorised morphing based on geometric changes. These categorisations ignored conventional technologies such as flaps, slats, landing gears, Concorde's variable incidence nose, Boeing X-53 (configured F/A-18) active aeroelastic wing, Dassault Mirage G sweep wing, Gevers Aircraft, Inc. Telescopic Wing, etc. names as Discrete Morphing. Therefore, categorisations based on geometric changes or mechanisms are not generic enough to handle all the forms of morphing. The authors believe that a more generic categorisation of morphing system is required based on the functionality, operational envelope, and application. So, the future of aircraft has the ultimate objective of what is called Continuous Morphing, where one system can provide multiple functionalities in a continuous adaptation along the flight envelope as we often see in Nature through birds, for instance. Ajaj *et. al.* [20] summarised the definitions and differences between Discrete and Continuous Morphing of which the more significant are shown in the Table 2.1.

Table 2.1: Definitions of Discrete and Continuous Morphing [20]

Discrete Morphing	**Continuous Morphing**
Singular functionalities	Multiple functionalities
Adopted locally on board the aircraft	Adopted all over the body of the aircraft
Operated at few points of the flight enveloped	Operated continuously along the flight envelope
Suppress coupling between the aircraft axes	Exploit couplings in morphing schedules and between the aircraft axes

2.1. Shape morphing of aircraft wings

Wings can be reconfigured by the resizing of span and chord length and by changing the sweep angle as depicted next. These changes are known as planform reconfigurations. Other ways of changing the aerodynamic behaviour of the wing is by recasting the wing out of its original plane or adapt the aerofoil profile. There are three types of out-of-plane rearrangements that can be described as chord-wise and span-wise bending and wing twisting. Figure 2.4 summarizes the morphing categories of wings.

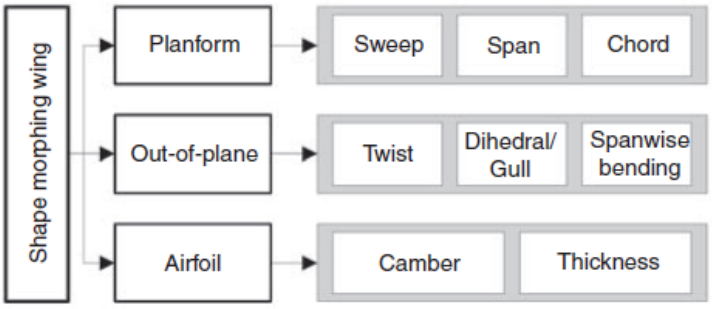

Figure 2.4: Categories of morphing wing [19]

In this section, morphing categories will be summarised and in the next sections of this chapter, relevant existing concepts and applications for this work will be described.

2.1.1. Wing planform change

The size and the planform geometry of the wing have a significant effect on the aerodynamic performance. If for different speeds the wing span and chord can be varied, then induced drag and/or parasite drag would be reduced in such a way as to increase lift-to-drag ratio at a given flight condition of the mission. Figure 2.5 shows the three forms of planform morphing. Of course combinations of these may be desirable.

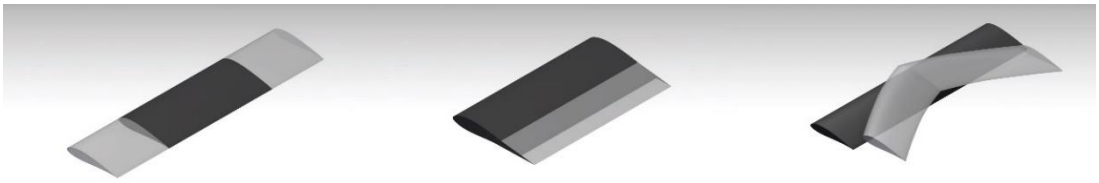

a) b) c)

Figure 2.5: In-plane shape morphing can be achieved by a) span change; b) chord length change; and c) sweep change

- Wing span variation

In terms of significant length change of the wing structure, telescopic structures have been used extensively because of its benefits. Telescopic morphing wings are sectioned longitudinally to form several segments with progressive reduction of the cross sectional area, such that each segment can be accommodated in the adjacent inner segment with minimum sliding clearance. Given the required length change, the number of segments can be determined. Another approach to change the wing span uses zig-zag or scissors-like mechanism for the wing-box. Besides these two technologies, a third is proposed, capable of independent span and chord changes by the use of extendable ribs and spars. Lead and screw mechanism and servo motors are used to create the linear displacements.

- Chord length variation

Very few researchers exploited the resizing of the chord length without using such flaps or slats. Currently, conventional aircraft or unmanned aerial vehicles (UAVs) are usually provided by lead and screw actuation systems for chord length resize. The application of smart materials, on the other hand, to achieve chord change is one of the least studied methods of wing morphing.

- Sweep angle variation

Pivoting of the wing has been the method of choice for the sweep change and has been implemented in many successful and operational aircraft. All the designs are composed by a pivoting mechanism supporting all the aerodynamic loads.

2.1.2. Out-of-plane transformation of the wing

A more dramatic way of changing the aerodynamic behaviour of the wing is by recasting the wing out of its longitudinal plane. Smart materials have been extensively explored through this approach. Figure 2.6 shows the three forms of out-of-plane morphing. Of course combinations of these may be desirable.

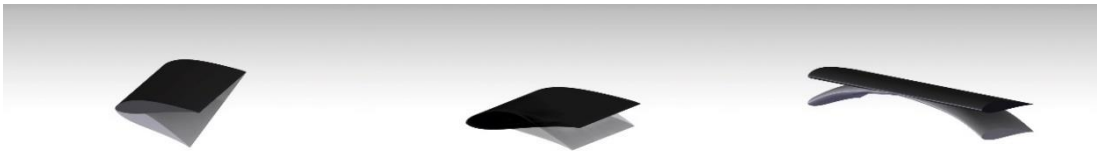

a) b) c)

Figure 2.6: Out-of-plane wing morphing is possible through a) wing twisting; b) chord-wise bending; and c) and span-wise bending

- Wing twist

Gradual changing of the aerofoil camber to create wing twisting can be achieved with sectioned wings in each segment can undergo out-of-plane shape changes by means of an eccentuator, a new concept in actuation. The eccentuator is a bent beam into a vertical and lateral translation at the other end. The vertical motion can then be delivered to the structure to flex it. Another approach is a flexible wing-box structure rigidly coupled to concentric outer and inner tubes, connected to servomotors, which are independently attached to different wing locations along the span. Torque rods can also be used to freely twist within metal sleeves attached bonded to the wing. Shape memory alloys can be used very efficiently to undergo twisting by asymmetric actuation of beams or SMA wires widely used for wing warping on the bottom of inflatable wings. Adaptive aeroelastic methods constitute another wing morphing wing approach where target shapes are met upon the application of aerodynamic loads on a variable stiffness wing structure. Piezoelectric actuators have been employed to manipulate the wing twist with the use of piezoelectric bimorph plates where an integrated flexible skin was free to rotate about the spar. Inflatable wings can change the twist angle with piezoelectric

actuators too via two different ways. The first is “bump flattening” and the second is piezo-benders.

- Aerofoil camber adjustment

Aerofoil camber can be uniformly changed along the span in similar manner to ailerons or, alternatively, gradual changes of the aerofoil camber along the span can create controllable twisting of the wing. Internal mechanisms, piezoelectric actuation or shape memory alloy actuation are used to perform the necessary camber change either by reconfiguration of the underlying structure or the morphing of the wing skin.

The most common concept of internal mechanisms is sectioning the ribs structure to finger-like sequential hinged segments. The camber line is modified by the successive rotation of the rib segments by means of pneumatic actuators. Compliant mechanisms are also being used as internal compliant systems. The leading and trailing edge are, also, reshaped by means of actuators. A different approach is the consideration of bi-stable plates inserted on the aerofoil section along the chord. By actuating the bi-stable plate the airfoil section is morphed between only two different stable shapes.

Piezoelectric actuators are used because of their unique and restricted job. The different concepts consist on the bending moment distribution by means of piezoelectric stacks or sheets or even tabs. In some cases, it was quickly found to be inappropriate because the targeted deflection was unachievable with the small induced strain of the best known piezoelectric stacks. Later on, some researchers tried to use mechanical amplifiers with multiple levers for the limited stroke of the piezoelectric actuators but it was discarded because of space limitation and the high flexural stresses at the mechanical amplification linkage.

Shape memory alloys actuators can also be used for trailing edge tip deformation. Although these materials only perform work with heating and cooling of the actuators, they can be used in many different ways, like their contraction can bend the trailing edge respectively, a par of one-way actuators in each, the contraction of one actuator upon heating, results in the extension of the other mechanically and, ultimately, shape memory alloy wire can be used in an antagonistic way to rotate the trailing edge. Some concepts are applied to the wing’s skin while others on the spars or even at the ribs.

- Spanwise wing bending

The research of a feasibility of a single-degree-of-freedom mechanism to morph a flat wing to a non-planar shape composed by a scissor-like mechanism can be used by means of the motion transfer of one linkage to the next with quaternary-binary links. SMA tendons and DC actuators can also be used as finger-like mechanisms to transfer the same type of motion that the previous concept can. Dihedral angle and gull configuration change are also considered for shape morphing aircrafts. Both former concepts consist in a two hinged segments wing in each the segments rotate with respect to each other and at the wing root with the use of electric actuators to fold the wing.

2.1.3. Aerofoil adjustment

Several researchers have explored the ways to alter the aerodynamic properties of the wing by reshaping the aerofoil profile without significant change of its mean camber line as represented in Figure 2.7. To reshape the aerofoil many concepts were examined starting with variable length trusses and internal mechanisms connected to compliant skin materials, SMA, SMA springs and wires, SMA actuation at the inside of an aerofoil, SMA linear actuators connected to a flexible skin through a cam based transmission system and, lastly, an out-of-plane piezoelectric actuator, called thin layer composite-unimorph ferroelectric driver and sensor (THUNDER).

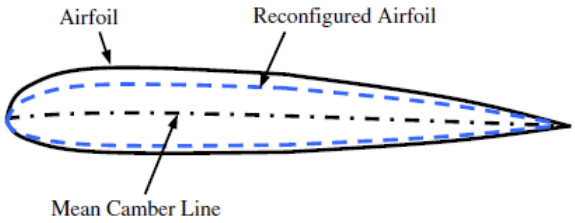

Figure 2.7: Aerofoil profile variation scheme [19]

The current work only concerns variable-span wings so only the planform sweep and span, and out-of-plane dihedral/gull changes will be discussed. Although sweep and dihedral or gull configurations change the effective span of the wing, these will be briefly discussed rather than the directly intended span changes, which will be the main focus.

2.2. Span morphing

Blondeau *et. al.* [21] designed and fabricated a three segmented telescopic wing for a UAV. Hollow fiberglass shells were used to preserve the span-wise aerofoil geometry and insure compact storage and deployment of the telescopic wing. To reduce the weight, they replaced the wing spars with inflatable actuators that could support the aerodynamic loads on the wing. Their telescopic spar design consisted of three concentric circular aluminium tubes of decreasing diameter and increasing length, connected by ceramic linear bearings, and deployed and retracted using input pressure. In a further development, Blondeau and Pines [22] adopted two identical telescopic spars instead of one mechanically coupled by the ribs, to prevent wing twist and fluttering. The new prototype could undergo a 230% change in aspect ratio, and seam heights were reduced giving less parasitic drag. In its fully deployed condition, the telescopic wing could achieve lift-to-drag ratios as high as 16, which was similar to its solid foam-core wing counterpart.

Monnera *et. al.* [23] performed wind tunnel tests on a model with telescopic wings actuated by two separate servomotors to study the effect of variable aspect ratio on wing-in-ground effect vehicles operating inside a channel. Changing the aspect ratio from 3.2 to 3.5 improved the lift-to-drag ratio more than the effect of both the ground and the sidewalls. Span changing also had a bigger advantage with walls present (up to 54.7% lift-to-drag increase compared to

the original wing). Wing tip extension does not control rolling moment efficiently on its own, but the influence of the ground or sidewall effects generates a positive rolling moment due to the high-pressure air trapped between the lower surface of the wing and the ground (or sidewall).

Table 2.2 shows that most of the vehicles used telescopic structures where the morphing partition(s) can slide in and out through the fixed inboard partition. These vehicles do not require any complaint or flexible skin, as the sliding/telescopic mechanism allows rigid covers and semi-monocoque construction.

Table 2.2: Air-vehicles that flew with span morphing technology [23]

Vehicle designation	Category	Morphing	Structure	Skin	Actuator
MAK-10	GA	Span	Telescopic	Sliding	Pneumatic
MAK-123	GA	Span	Telescopic	Sliding	Pneumatic
FS-20	Glider	Span	Telescopic	Sliding	Screw jacks
FLYRT	UAV	Span	-	-	-
Virginia Tech	UAV	Span	Telescopic	Sliding	Rack and pinion
MFX-1	UAV	Aspect ratio and Sweep	Articulated lattice structure	Stretchable	-
Olharapo	UAV	Span	Telescopic	Sliding	Rack and pinion

Beyond the concepts already mentioned, the morphing unmanned aerial attack vehicle, developed by AeroVisions International Inc.[2] [24] within the Morphing Aircraft Structures program funded by DARPA, consisted of several sliding segments. The wingspan was inversely proportional to the cruise speed, and allowed for several operating conditions from loitering to fast cruise to high-speed attack.

A different approach was disclosed by Arrison *et. al.* [25] that modified a Delta Vortex RC aircraft by adding telescopic wings. The RC vehicle was successfully flown, and it highlighted a change in static stability between the retracted and extended case of nearly 5%.

In the work from reference [26], a flexible skin is used to achieve the span variation capability. The wing supporting structure is composed by a zero-Poisson cellular honeycomb. This core is reinforced with pultruded carbon fibre rods. An elastomeric skin is used to close the cellular core and give the final aerodynamic shape. This methodology was tested for a span variation of up to 100%.

[2] Experimental aircraft consulting, design and construction.

Ajaj *et. al.* [27] developed the zigzag wing-box concept which allows the wing span to extend or retract by means of actuators and consists of a rigid part that is a semi-monocoque construction and a morphing part composed by various morphing partitions and in each partition there are two spars each consisting of two beams hinged together as seen in Figure 2.8.

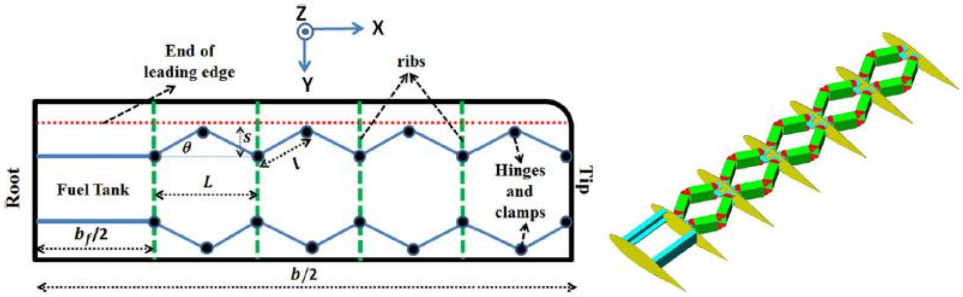

Figure 2.8: Zig-zag wing-box concept top view (at left) and isometric view (at right) [27]

A flexible skin bounded by two ribs through which the spars are connected is used to cover each partition. The semi-monocoque structure houses the fuel tank and transfers the aerodynamic loads from the morphing part to the fuselage. The ribs transfer the loads between the spars of adjacent morphing partition and serves as the main structure to which the flexible skins are to be attached. The zigzag wing-box concept is then incorporated in the rectangular wing of a medium altitude long endurance (MALE) UAV to enhance its operational performance and provide roll control and replace conventional ailerons.

Distributed actuation is adopted to allow the wing span of any partition to be controlled independently of the adjacent partitions. Four possible configurations are considered for the installation of the distributed actuators into the Zig-zag wing-box. Figure 2.9 shows an overview of the four arrangements considered.

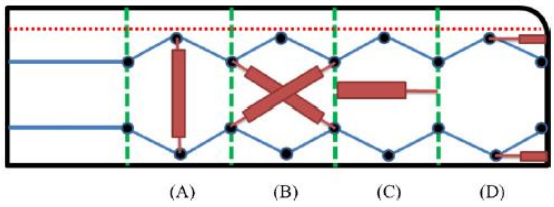

Figure 2.9: Actuator configurations; (A) vertex to vertex; (B) crossed; (C) direct driving; and (D) rib to vertex [27]

The concept is heavier than the conventional wing-box but can still provide an endurance benefit of 5.5%. One major difficulty with complaint morphing concepts is that the skins have to be flexible to allow structural deformations and thus they cannot withstand large aerodynamic loads but do provide a smooth aerodynamic surface. This prevents complaint morphing concepts from having the structural benefits of semi-monocoque construction and requires a heavier internal structure (spars and ribs) to withstand the loads.

A telescoping wing for flight speed adaptation was developed and manufactured using fused deposition modelling technology [28]. The wing structure is made of a thermoplastic printed

material reinforced with carbon fibres. The actuation mechanism is fitted within the central wing-box which also serves to attach the wing to the fuselage. The wing fitted to an all printed UAV called Variable Airspeed Telescoping Additive Unmanned Air Vehicle (VAST AUAV) is shown in Figure 2.10.

Figure 2.10: 3D printed telescoping wing [28]

Felício *et. al.* [29] developed and validated a variable-span morphing wing through graphical CAD/CAM tools intended to be fitted to a small UAV prototype (named Olharapo). The wing is built in composite materials and is made of two parts. The inboard part is fixed to the fuselage and uses a monocoque skin construction. The outboard part slides inside the inboard part to change the span of the wing and uses a typical structure made of spar, ribs and thin skin. An electro-mechanical actuation mechanism is developed using an aluminium rack and pinion system driven by two servomotors placed at centre of the wings. Figure 2.11 shows the CAD model and a detail of the wing's variable span system.

a) b)

Figure 2.11: Wing central bay: (a) CAD model and (b) wing prototype. 1) servo motors supporting board; 2) board linkage; 3) wing-fuselage lug; and 4) upper board and actuation bay [29]

2.3. Various combined in-plane morphing capabilities

Alemayehu *et. al.* [30] designed and constructed a wing-box mechanism capable of changing wing span, chord and sweep by means of actuators and servos, and an electric motor powering screws (which can be seen at Figure 2.12 b) highlighted by red arrows). The mechanisms used to accomplish all these intended motions can be seen in Figure 2.12 and Figure 2.13.

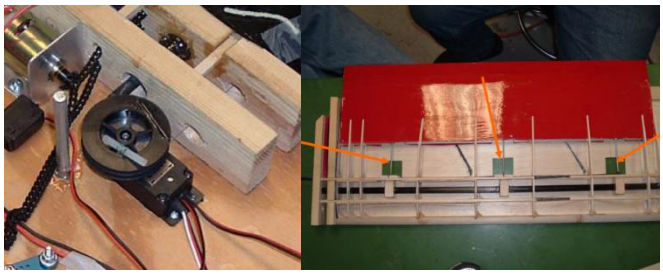

a) b)

Figure 2.12: Span and chord setup (The red arrows point to the three power screws) [30]

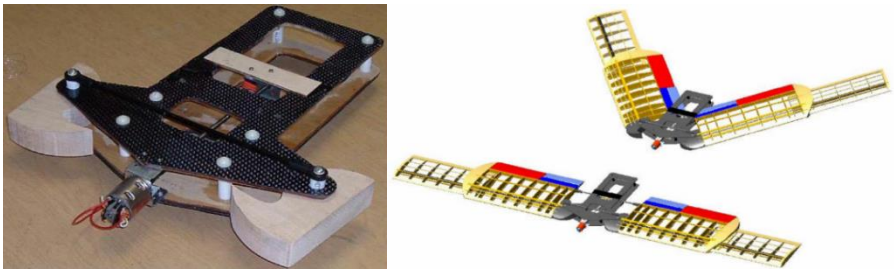

a) b)

Figure 2.13: Wing-box mechanism a) sweep mechanism after construction and b) CAD drawing of wing-box with wings [30]

NextGen Aeronautics [31] developed an UAV, called the MFX-1 and referred to as the Bat-Wing, with a wing that could undergo significant sweep changes during flight. An electric motor deformed an endoskeleton wing-box structure that was covered with an elastomeric skin with out-of-plane stiffeners. Later the second-generation MFX-2 is a twin-jet, 135kg (300lb) UAV than can be switched between remote and autonomous control in flight. An articulating structure and flexible skin enables a 40% change in wing area, 73% change in span and 177% change in aspect ratio, says NextGen. Unlike conventional variable-geometry wings, morphing allows area and sweep to be varied independently to optimise the configuration for multiple flight regimes.

Vale [32] developed a concept that integrates aerofoil camber change with a telescopic span variation concept. The telescopic wing is made of two elements, one that slides inside the other by means of a pull-pull cable and pulleys. The inner and outer aerofoil sections must always be deformed in a similar fashion to allow the telescopic motion to occur. The wing skin is supported by carbon fibre ribs whose contour thickness is tailored to allow shape changes between a symmetrical aerofoil and a cambered aerofoil. Between these ribs, the skin is made of balsa wood and a circular spar at the leading edge provides bending stiffness and strength. Rib deformation is achieved by rotating screws actuated by small electrical DC motors that make the open trailing edge upper skin slide chordwise in the opposite direction to the lower skin. The aerofoil mechanism of the inner rib is placed inside the wing and that of the outer rib is placed outside the wing.

Gamboa *et. al.* [33] designed a morphing wing concept for a small experimental unmanned aerial vehicle to improve the vehicle's performance over its intended speed range. The morphing concept is based on changes in wing-planform shape and wing-section shape achieved by extending spars and telescopic ribs. Variable span, variable chord and variable airfoil shape are the geometric parameters that can be changed. The concept presented does not use adaptive materials; it uses an adaptive internal structure built with conventional materials that are covered with a flexible skin for the aerodynamic shape. Unlike the NextGen bat wing, which has a sweep/chord variation coupling that makes its flexible skin withstand in-plane deformation without altering the airfoil thickness, this concept changes the thickness by out-of-plane actuation on the skin. The proposed mechanism tries to produce both chord and span morphing, while allowing changes in the wing airfoil, either by simply scaling the wing airfoil according to the new chord or by actually changing the complete geometry of the airfoil. It consists of a telescopic rib that is actuated by a rotational device that drives screws, causing displacement on the outer skin of the wing section. The amount of displacement in each station of the rib is determined by the screw pitch and the allowable number of rotations that the screw can take at that station. The shape of the airfoil (chord length and thickness distribution along the chord) must therefore be known previously to the assembly of the mechanism, and this is why the optimization process is needed before the design of the morphing mechanism is completed.

2.4. Sweep morphing

Marmier and Wereley [34] built and tested in a wind tunnel a variable-sweep UAV. A pair of antagonistic inflatable bellow actuators were embedded in a cylindrical polyvinyl chloride fuselage and controlled by solenoid valves that allowed wing sweep to vary between 0 and 45 degrees. Slide rods guaranteed a smooth translation.

Neal *et. al.* [35] provided a sweeping mechanism for their shape-morphing UAV that was actuated by means of two electromechanical, lead-screw actuators via a three-bar linkage. Neal et al. also implemented a variable-geometry tail and increased the structural strength.

Mattioni *et. al.* [36] investigated a variable-sweep wing concept based on bi-stable composite spars. The wing-box in their design consisted of two spars with an interconnected truss-rib structure. Each spar had a significant transverse curvature, which increased the bending stiffness and also allowed the spar to behave like an elastic hinge under high drag loads. The design could eliminate hinges and mechanisms, but could suffer from fatigue. No skin was included and adding a skin could interfere with the snapping motion.

2.5. Folding wings

The best-known UAV that performs dihedral and gull variations is the Lockheed Martin z-wing UAV [37] that performs a foldable movement of the wing where the span length, aspect ratio, and effective sweep angle may be varied where the span length, aspect ratio, and effective sweep angle may be changed (Figure 2.14). The folding wing design incorporates hinged

joints at two span-wise stations enabling rigid body motion of four primary wing sections. Two approaches to fold the wing were investigated: a thermo-polymer actuator driving a helical spline gear or electro-mechanical rotary actuators. However, the helical spline approach was high risk and hence electrical actuators were used. A morphing UAV aircraft was successfully flight tested.

Figure 2.14: Progressive foldable wing of Lockheed Martin's concept [37]

A similar prototype was built by Subbarao *et. al.* [38] which consisted on a mechanism to continuously morph a wing from a lower aspect ratio to higher and to further extremities of a gull-configuration and an inverted gull-configuration with a sliding extendable wing portion with rack and pinion and dc motor mechanism. The mechanism comprises of a linear actuator for the extension of the wing and the servo motors to obtain the gull and inverted gull configurations.

2.6. Wing-box structural analysis

Before starting the structural analysis and, mostly, the parametric study, previous publications and researchers of similar projects have been consulted in order to take the best approach to systems developed in a CAD/CAM tool. After the parametric study, numerical computation was used to interpolate results.

Santos *et. al.* [39] performed the structural design of a composite variable-span morphing wing intended to be installed on a small UAV to provide high flight efficiency in an extended operational speed range, relative to a conventional fixed wing, by symmetrically adjusting the wing span to the flight speed. The focus was on three distinct parts: first, structural layout definition according to the morphing concept constraints and the materials used; second, design for static loads using the finite element method (FEM) where strength, stiffness and weight are key design parameters; and third, experimental testing of a prototype of the wing. Results evidence that the design has good stiffness and strength characteristics and that the numerical predictions correlate well with the experimental tests.

Gamboa *et. al.* [40] lead a study concentrated on the flutter critical speed estimation because of the effects arising due to the interface between fixed and moving wing parts. Although the former objective is not related with the current study of this work a modal analysis made with ANSYS Structural APDL (Ansys Parametric Design Language) for obtaining mode shapes and natural frequencies can be helpful for the use of the same software and future work. The critical flutter speed was computed using the typical section in aeroelasticity with unsteady

linearized potential theory together with the three-dimensional lifting surface strip theory approximation for lifting surfaces with high aspect ratio. The flutter analysis allowed to conclude that the wing can fly safely within the intended speed envelope because the critical flutter condition is well above the maximum flight speed.

3. Preliminary design

The work in this chapter was not performed by the author of this dissertation alone but also by the different working groups of the CHANGE project partners. The UBI group had a big contribution of the work described in this chapter with the author´s collaboration. The structural concept and actuation mechanism were developed by others within this UBI group.

As decided by all partners within the CHANGE project, it is important that the various wing components/mechanisms of the wing should be independent. This approach can facilitate the development of each required mechanism as well as making the integration of all parts easier. According to the shape changes required, the wing cross section is divided into three parts: leading and trailing edge surfaces, and wing-box. Each part contains its own actuation system within its bounds, such that the telescopic motion mechanism is placed inside de wing-box without restrictions.

3.1. Telescopic wing concept

3.1.1. Design loads

As specified in EASA's[3] Certification Specifications for Very Light Aeroplanes CS-VLA [41] the design loads are estimated using V-n diagrams which allow to obtain the symmetrical load factor envelope for any given wing configuration as a function of speed.

All wing configurations have a mean chord of 0.6 m and it is assumed that the maximum and minimum manoeuvre load factors in any wing configuration are +3 and -1.5, respectively. It is also assumed that the cruise speed for the fully extended wing is the defined take-off speed and that the minimum lift coefficient (maximum negative value of C_L) is half the maximum lift coefficient. The wing aerodynamic data used to compute the load factors is presented in Table 3.1. The calculations made to obtain the n-V diagrams involve two separate diagrams, of which the first is composed. These two diagrams (the manoeuvre and the gust diagrams) are added together to form the final diagram where the most critical segments from both diagrams prevail, limited by the stall load factor. Usually, for non-passenger aircraft, it is not considered the design speed for maximum gust intensity, V_B, so only V_C, V_D and V_S which are cruise speed, design dive speed and stall speed, respectively, were considered along with the respective wing data values obtained from XFOIL (such as the maximum lift coefficient, lift-curve slope, wing area, design speed, stall speed, etc.).

The combined V-n diagrams obtained are superimposed in Figure 3.1. It is seen that, for the fully extended wing, the critical envelope takes place for the loitering phase. The high-speed envelope shows higher speeds and load factors than predicted and must be considered in the

[3] European Aviation Safety Agency

wing's structural sizing. It can also be noticed that the critical envelope, at all flight phases, is the gust envelope.

Table 3.1: Required data to compute the V-n diagrams

Wing configuration	Wing area [m^2]	Maximum lift coefficient ($C_{L\ max}$)	Minimum lift coefficient ($C_{L\ min}$)	Lift curve slope [rad^{-1}]	Cruise speed [km/h]
Take-off	2.4	1.42	-0.71	4.297	76
Loiter	2.4	1.56	-0.78	4.167	76
High-speed	1.8	1.38	-0.69	3.82	110
Landing	2.4	1.53	-0.765	4.167	76

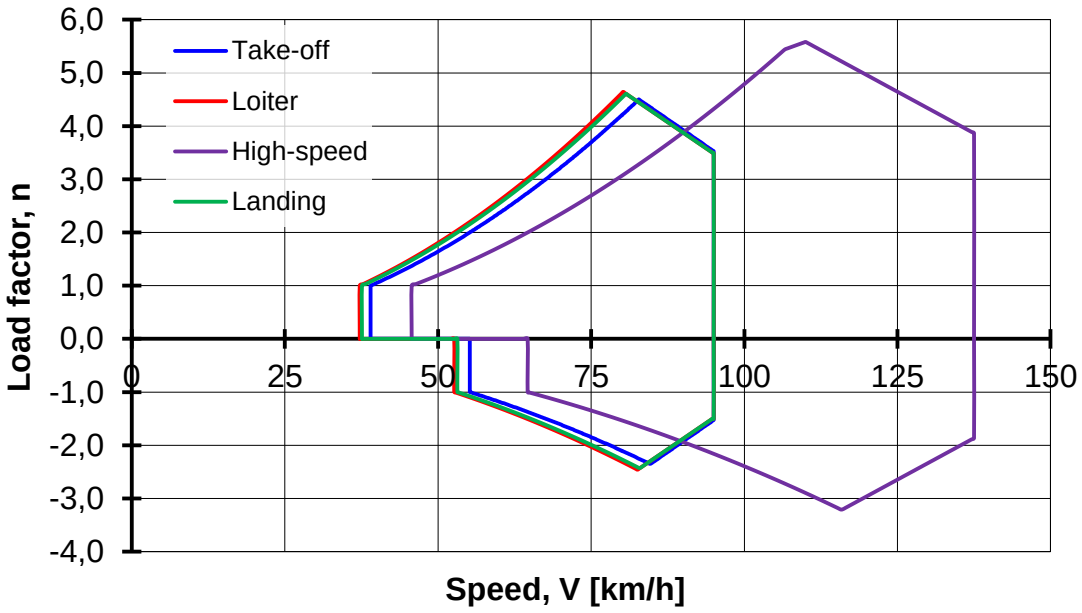

Figure 3.1: Combined V-n diagrams

For the loiter and high speed V-n diagrams the positive limit load points are extracted, considering a low speed, high load factor and high angle of attack case and a high speed, high load factor and low angle of attack case. As said earlier, the gust load factors must be computed as described in EASA CS-23 certification specifications from pages 1-C-2 to 1-C-5. From the values of speed and load factor, the wing's lift coefficient (C_L) is calculated as follows in equation 3.1:

$$C_L = \frac{m\ g\ n}{\frac{1}{2}\ \rho\ V^2\ S} \tag{3.1}$$

Where:

m = Full span wing's mass [kg]

g = Acceleration due to gravity [m/s^2]

n = Load factor

ρ = Density of air at the altitude considered [kg/m^3]

V = Aircraft equivalent speed [m/s]

S = Wing area [m^2]

Then, from the lift and drag coefficient curves and the pitching moment coefficients obtained from the XFOIL analysis, the corresponding angle of attack and drag coefficient are acquired. Finally, lift, drag and pitching moment are calculated for the given speed and wing area as follows in equations 3.2, 3.3 and 3.4:

$$L = \frac{1}{2}\,\rho\,V^2\,S\,C_L \quad ,N \tag{3.2}$$

Where:

ρ, V, and S are referred to in equation (3.1)

C_L = Wing Lift coefficient

$$D = \frac{L}{\frac{C_L}{C_D}} \quad ,N \tag{3.3}$$

L and C_L are referred to in equation (3.2)

C_D = Wing Drag coefficient

$$M = \frac{1}{2}\,\rho\,V^2\,S\,C_m\,0.6 \quad ,Nm \tag{3.4}$$

Where:

ρ, V, and S are referred to in equation (3.1)

Cm = pitching moment coefficient

All these values are summarized in Table 3.2, next.

Due to the negative load factors being much lower than the positive ones, those will not be considered for the wing-box sizing.

Since lift and drag are perpendicular and parallel, respectively, to the free stream direction, they are rotated by the angle of attack to give vertical and horizontal components, perpendicular and parallel to the wing chord line, respectively. The loads used to size the wing-box are shown in Table 3.3.

Table 3.2: Load cases for wing-box preliminary sizing

	Loiter		High-speed	
	Low speed	**High speed**	**Low speed**	**High speed**
Speed [km/h]	80	95	110	137.5
Load factor	4.64	3.49	5.58	3.86
Lift coefficient	1.567	0.835	1.329	0.589
Drag Coefficient	0.17	0.048	0.14	0.035
Angle of attack [°]	17	4.48	18	6.84
Moment coefficient	-0.17	-0.185	-0.02	-0.06
Lift [N]	1138	854	1368	948
Drag [N]	123	49.1	144	56.3
Pitching moment [Nm]	-74	-114	-12.4	-57.9

Table 3.3: Loads for wing-box sizing

	Loiter		High-speed	
	Low speed	**High speed**	**Low speed**	**High speed**
Vertical load [N]	1124	856	1346	947
Horizontal load [N]	-215	-17.7	-286	-56.9
Torsion moment [Nm]	-74	-114	-12.4	-57.9

3.1.2. Wing-box concept

From the wing shape optimization performed by Aerodynamics Research Association (ARA), partner in the CHANGE project, three aerofoils were taken into account for the final decision of choosing one as the reference to define a rigid wing-box. NACA 2510, NACA 3510 and NACA 6510 were thoroughly analysed and was decided by all CHANGE partners that the wing-box should start at 30% of the chord and would extend to 70% of the chord using the NACA 6510 aerofoil, extending 40% of the total chord length. A comparison of the three aerofoils is shown in Figure 3.2.

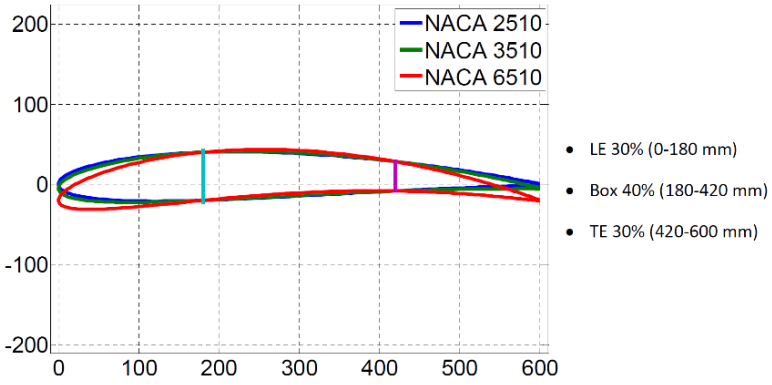

Figure 3.2: Wing-box section definition (dimensions in mm)

From the analysis it was concluded that the aerofoil NACA 6510 performance exceeds the other two for two of the concerned mission's phases. Its better lift-to-drag ratio and a higher maximum lift coefficient are two of the most important factors and with its optimization mission's phases like loiter and landing are significantly improved. These were the main reasons that lead to the final choice of the aerofoil. Although the aerofoil NACA 3510 performed better in the take-off and the NACA 2510 in the high speed cruise mission's phase, the mission's phase that takes longer is the loiter and, as said earlier, the aerofoil NACA 6510 outperforms the other concerned aerofoils in this mission's phase and also at the landing phase.

An interesting fact is that the three aerofoils intersect at 30% and 70% of the chord, as we can see from the Figure 3.2, which makes the decision of choosing the aerofoil easier and the leading and trailing edges, as are distinct mechanisms, can be manufactured with no restrictions from the wing-box.

Since it is necessary to ensure the geometrical compatibility between the IFW and OMW, the aerofoil of the sliding portion is built as an offset from the fixed portion aerofoil geometry. This offset is necessary to account for the sandwich skin thickness. This leads to a slightly different geometry of the local aerofoil when compared with the original NACA 6510. The original NACA 6510 and the modified version are shown in Figure 3.3. The original NACA 6510 has a relative thickness of 10 % and a relative camber of 6 %. The modified aerofoil has slightly reduced thickness and camber, being 9.58 % and 5.94 %, respectively.

Figure 3.4 shows the general dimensions of the wing planform and indicates where each aerofoil is to be used. Owing to the offset of the NACA 6510_mod aerofoil the local chord length of the OMW is only 578 mm.

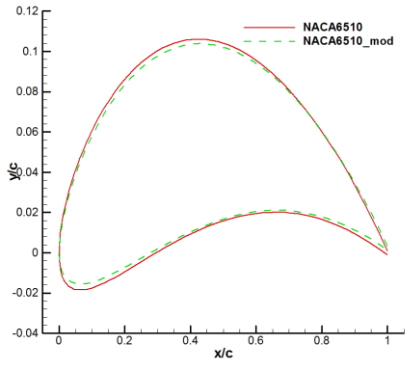

Figure 3.3: Wing-box aerofoils

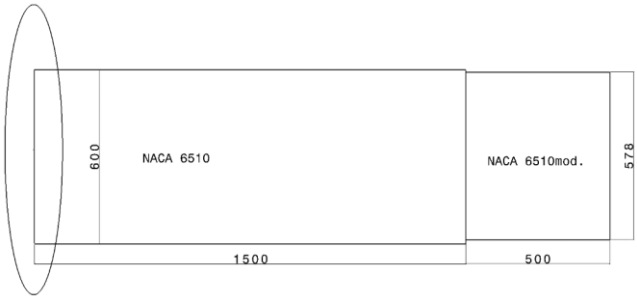

Figure 3.4: Wing planform and its aerofoils (dimensions in mm)

With everything well-marked, a wing-box prototype was made of a composite sandwich skin with embedded spar caps in the corners as shown in the sketch of Figure 3.5. This wing-box is built in two compatible pieces: the wing-box of the inboard fixed wing (IFW) and the wing-box of the outboard moving wing (OMW) which fits and slides inside the inboard fixed part. The webs (vertical elements of the wing-box) of the IFW do not extend its full span as the spar caps do. Instead, they are interrupted at one meter from its root to allow the OMW to retract into the IFW as can be seen in Figure 3.12 later in this section.

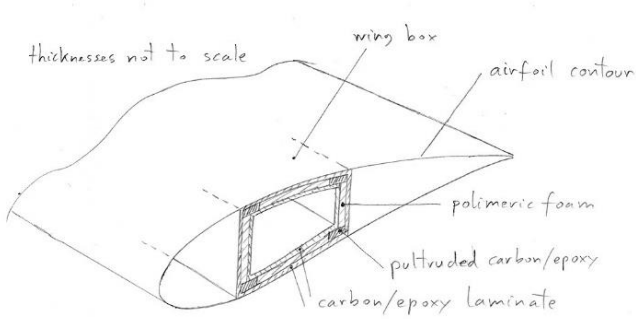

Figure 3.5: Wing-box concept

The wing-box of each of the IFW and OMW become single parts after manufacturing. Then, either the wing-box is bonded to the skin, if the skin can be built in one or two pieces (upper and lower skins for example), or the leading and trailing edge surfaces are connected onto it if they are fully separate modular systems, making the wing-box the core component. All wing configurations have a mean chord of 0.6 m.

The Aircraft Research Association (ARA) proposed a modification to the wing tip of the initial design. In order to reduce the local lift coefficient at the wing tip and consequently the induced drag produced by the wing with the aerofoil NACA 6510, the use of the aerofoil NACA 0010 at 0.2 m distance from the tip was suggested. The change from the aerofoil NACA 6510_mod to the NACA 0010 only affects the OMW. Because this shape transition is no longer compatible with the retraction into the IFW wing, the telescopic extension motion would reduce to only 0.4 m rather than the initial 0.5 m and the IFW semi-span would reduce to 1.4 m. The fully retracted semi-span would change to 1.6 m but the total semi-span would remain at 2 m and the morphing LE and TE devices outer position limit would still be 1 m. Figure 3.6, shows the final dimensions of the wing-box which were later implemented at the detailed design.

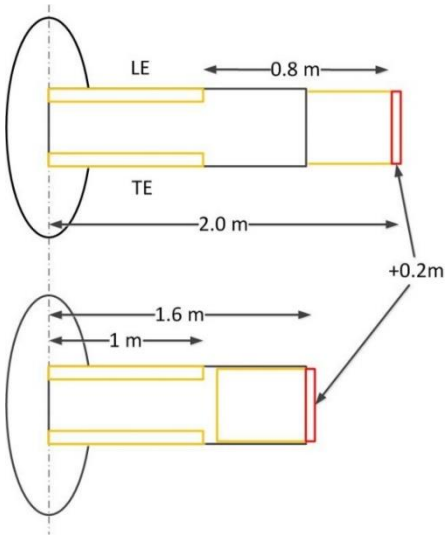

Figure 3.6: New proposed wing planform (dimensions in m)

Even though, this modification reduces the fraction of wing span variation, which may reduce the performance benefits of the telescopic wing concept, there is no foreseen problem in terms of the wing's structural design.

3.1.3. Materials

The wing-box is composed by three materials. Carbon fibre fabric with epoxy constitutes the sandwich faces, and among these, foam (Airex®[4] C70.90) making it the core of the sandwich. To fill a small gap of less than 1 mm at the corners of the composite sandwich, pultruded unidirectional carbon fibre with epoxy was used for the spar caps. The properties of these materials are presented in Table 3.4.

Note that the properties of the sandwich faces are assumed for a hand lay-up procedure with vacuum curing.

[4] Airex® Foams, retrieved from: http://www.corematerials.3acomposites.com/airex-c70.html, 30/10/13.

Table 3.4: Material properties

Property[5]	Wooven carbon/epoxy	Pultruded carbon/epoxy	Airex® C70.90 foam
ρ, kg/m^3	1500	1600	100
E_1, GPa	46	105	0.065
E_2, GPa	46	7.5	0.065
G, GPa	3.5	3.75	0.034
v_{12}	0.1	0.3	0.0227
v_{21}	0.1	0.3	0.0227
F_{tu1}, MPa	600	1500	2.7
F_{tu2}, MPa	600	50	-
F_{cu1}, MPa	570	1200	2.0
F_{cu2}, MPa	570	250	-
S_{12}, MPa	90	70	1.7

3.1.4. Actuation system

The actuation system is fully contained inside the wing-box thus avoiding any interference with other components and enabling the modularity of the morphing wing design. In Figure 3.7, we can see the three parts already referred earlier in this chapter such as the different morphing devices and the wing-box morphing mechanism. This mechanism is composed by a pinion and rack system actuated by a DC motor. The motor is mounted on a plywood rib of the OMW and the rack is connected near the wing root, allowing the DC motor to push/pull the OMW only in the spanwise direction. To reduce the sliding friction between the IFW and OMW, thin polytetrafluoroethylene (PTFE) linear bearings were later added to the design. The former are bonded inside the IFW and to the outside of the OMW at the corners of the wing-boxes. The PTFE bearings are bonded using acrylic glue specially designed for low surface energy plastics, thereby ensuring good adhesion to the wing-boxes corners.

[5] Subscripts 1 and 2 denote the direction of the fibre and perpendicular to the fibre, respectively, where applicable.

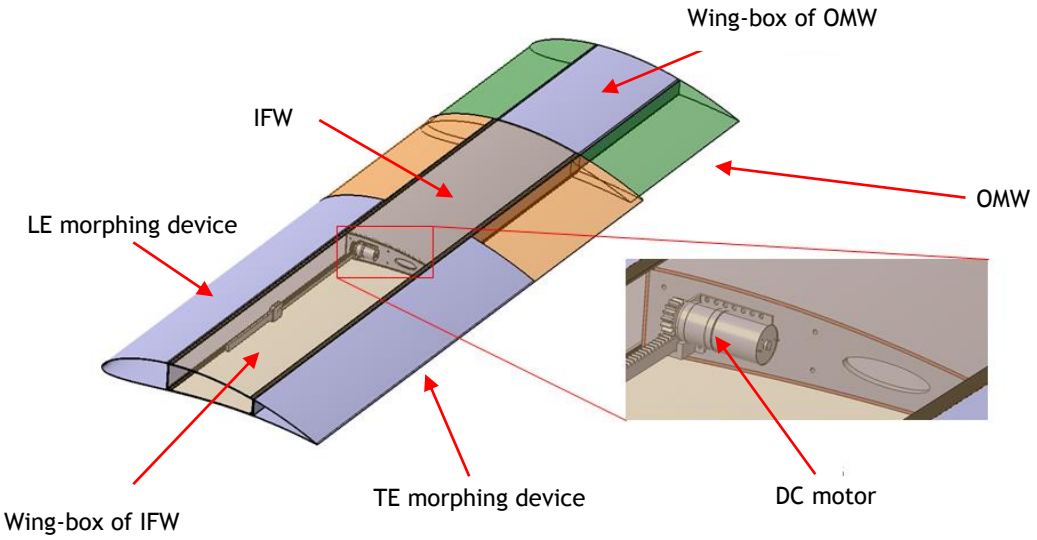

Figure 3.7: CAD Design of the actuation mechanism

The brushed DC motor has a gear ratio of 99:1 and delivers a stall torque of 1.13 Nm and a no-load speed of 100 RPM, at 6 V. In order to have a feedback position of the wing a 10 turn 5 kΩ potentiometer, that is connected to the motor controller board together with the DC motor, is used. The DC motor, feedback potentiometer and motor controller makes up the servo actuation system.

From Figure 3.8 is possible to notice the linear PTFE bearings bonded to the inside of the IFW and to the outside corners of the OMW, and the inboard and outboard moving wing-boxes as distinct parts, as referred earlier.

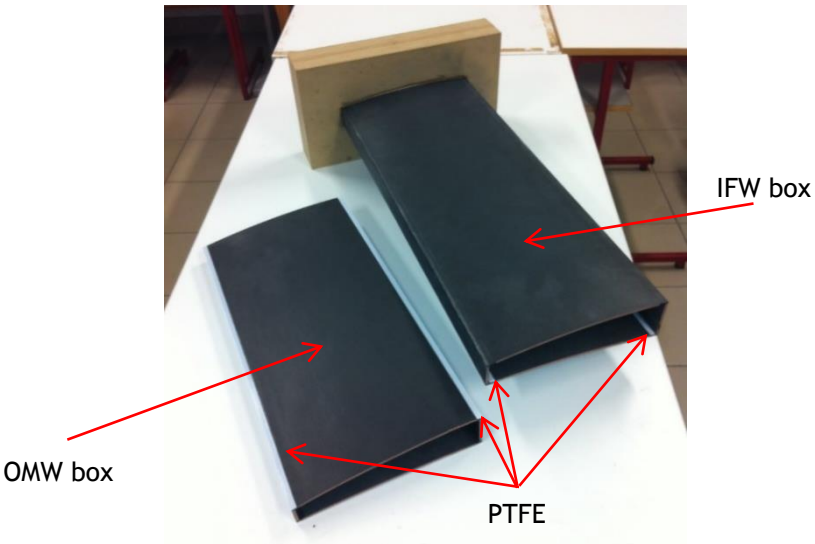

Figure 3.8: Detailed view of IFW and OMW prototype. Notice the linear guides bonded to the corners of both components

The pinion and the rack are made of oil filled nylon (Ertalon LFX[6]). This material is especially suitable for this type of application because of its low weight and low friction coefficient. Since the proposed mechanism is only intended to perform wingspan variations (and not roll manoeuvres through wing asymmetric extension), the pinion is designed so that the OMW actuation speed is about 100 mm/s. This calculation resulted in a pinion with a diameter of 20 mm and a modulus of 1.25. The chosen modulus offers a good compromise between the number of teeth that ensures a smooth torque transfer and the manufacturing simplicity. The control of the wing variation is done with a pulse width modulation (PWM) signal, generated by common radio control systems. The signal is injected in the motor controller board that ensures the wing extends to the desired wingspan configuration.

A prototype of the telescopic wing-box was built to develop the actuation mechanism and validate the structural concept. From Figure 3.9 it can be seen the OMW rib to which the DC motor, the motor controller and the feedback potentiometer are installed. The rib can be easily detached from the OMW by removing 6 screws, greatly simplifying the maintenance of the actuation components.

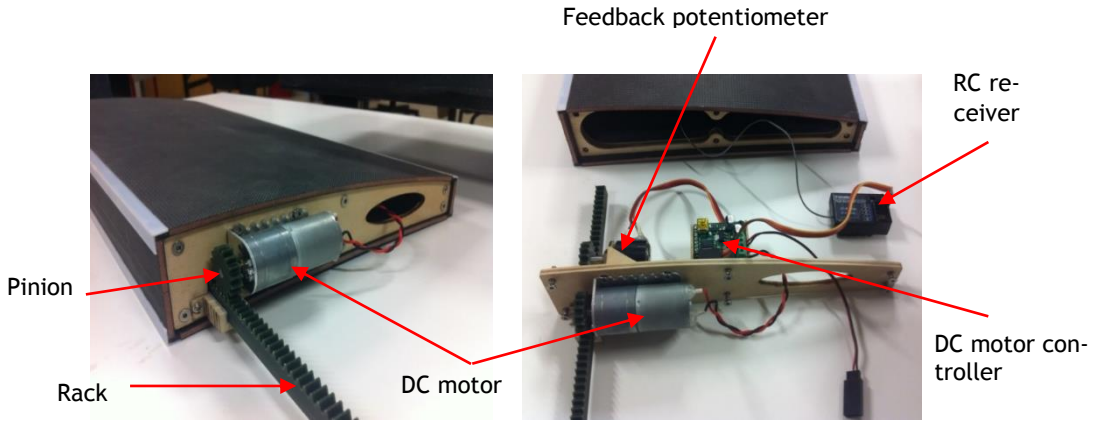

Figure 3.9: Detailed view of the actuation system: a) assembled and b) disassembled

3.1.5. Preliminary wing-box design

From the previous results it is clear that the wing-box has the required strength and stiffness. In some regions the stress intensity is substantially high but localized reinforcements can be made to refine it. The high stiffness is obtained because the minimum laminate thickness assumed is 0.12 mm (for practical reasons) favouring the good functioning of the telescopic wing, preventing it from bending and twisting too much, that could cause increased friction between the inside of the IFW and the outside of the OMW when it moves. On the other hand, the mass of the component is also influenced as we increase laminate layers to stiffen it.

6 Internally lubricated cast nylon. Data sheet retrieved from: http://www.quadrantplastics.com/fileadmin/quadrant/documents/QEPP/EU/Product_Data_Sheets_PDF/GEP/Ertalon_LFX_PDS_E_25012011.pdf, 10/09/2014

After sizing the wing-box configuration, the final dimensions and weight of the proposed wing-box can be summarized. The cross-sections with the main dimensions of the inboard fixed wing and outboard moving wing are shown in Figure 3.10 and Figure 3.11, respectively.

In summary, the wing-box structural components of the IFW have the dimensions and materials as shown in Table 3.5.

Table 3.5: Wing-box component dimensions and materials for IFW

Component	Component	Dimensions [mm]	Material
Spar cap	-	11 x 2	Pultruded carbon/epoxy
Vertical sandwich	Skins laminate Core	0.12 2	Woven carbon/epoxy Airex® C70.90
Horizontal sandwich	Skins laminate Core	0.24 3	Woven carbon/epoxy Airex® C70.90

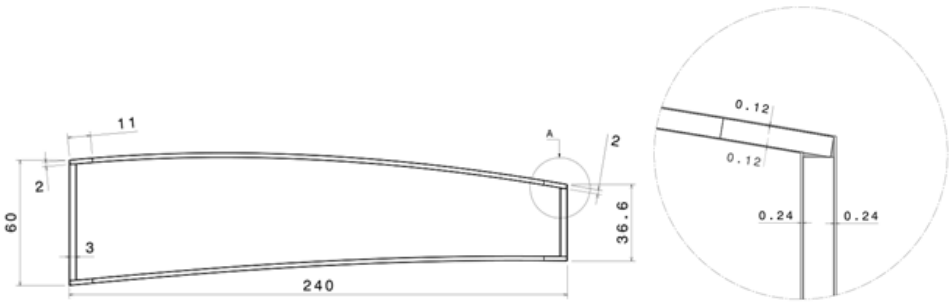

Figure 3.10: Inboard fixed wing cross section showing structure dimensions (in mm)

The wing-box structural components of the OMW have the dimensions and materials as shown in Table 3.6.

Table 3.6: Wing-box component dimensions and materials for OMW

Component	Component	Dimensions [mm]	Material
Spar cap	-	5 x 2	Pultruded carbon/epoxy
Vertical sandwich	Skins laminate Core	0.12 2	Woven carbon/epoxy Airex® C70.90
Horizontal sandwich	Skins laminate Core	0.12 3	Woven carbon/epoxy Airex® C70.90

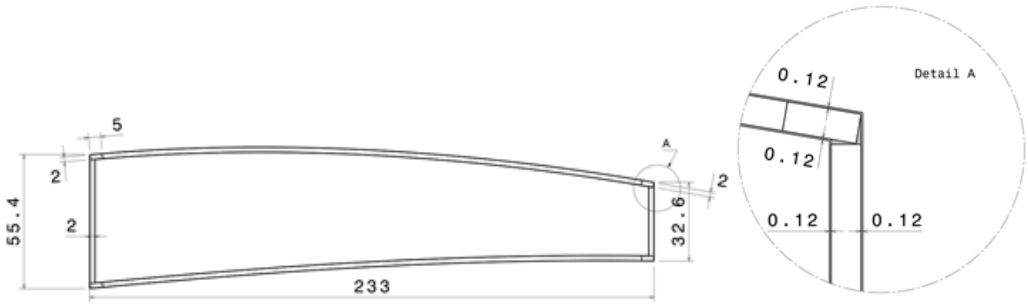

Figure 3.11: Outboard moving wing cross section showing structure dimensions (in mm)

In Figure 3.12 it can be seen the span of the IFW and the extension of its wing-box webs, and the OMW explained dimensions. The interrupted webs mentioned earlier in this section can also be seen on one side. While the IFW has a total length of 1500 mm the OMV has 1150 mm. The latter has 650 mm embedded in the IFW, of which 500 mm are inside of the IFW with the interrupted webs. At an inner part, 150 mm are allocated inside the IFW which has webs.

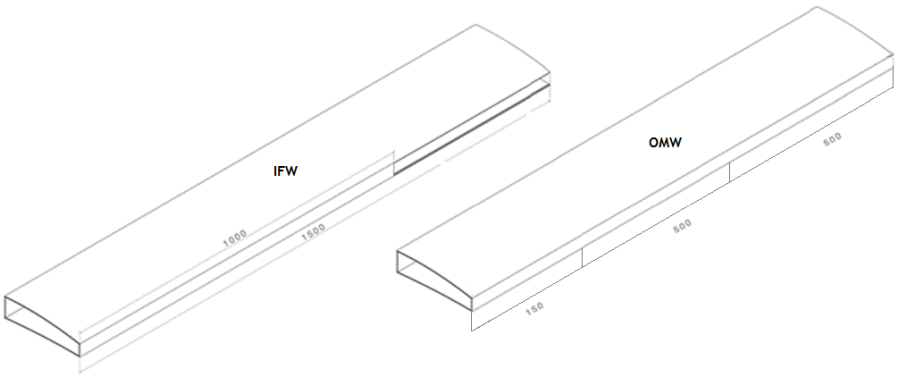

Figure 3.12: Inboard fixed wing and Outboard moving wing structure dimensions in mm (not to scale)

In Figure 3.13, a general CAD model of the telescopic wing-box in its retracted and extended configuration is shown. It is possible to observe the seamless interface between the two portions and also the very small gap that is created using the current approach. In fact the discontinuity between the two parts is directly related to the IFW skin thickness. Therefore, minimizing the latter not only helps to minimize the wing-box weight, but also reduces the gap. It is also noticeable the interrupted webs of the IFW.

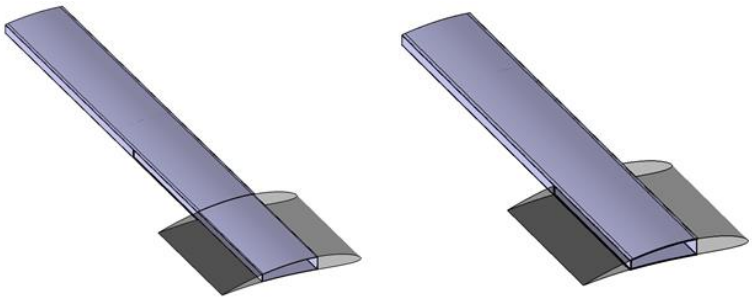

a) b)

Figure 3.13: CAD Model of the telescopic wing-box: a) extended configuration and b) retracted configuration (OMW skin added for clarity)

Table 3.7 presents the wing-box estimated mass for each part of the wing and the prototype wing-box total mass with the implemented actuation system. It is expected that the IFW is heavier than the OMV since it is responsible for supporting the loads transmitted by the latter. The estimated total mass of the telescopic wing-box structure for the two wings is 2.3 kg but the overall mass is quite sensible given the complexity of the wing-box and its fabrication as we can verify. In the prototype, due to material availability, a core thickness of 3 mm instead of 2 mm of foam was used in the skin sandwiches.

Table 3.7: Wing components mass (relative to one wing) from the FE model and prototype built

Component	**Estimated wing-box**		**Prototype wing-box**	
	Mass, Kg			
IFW	0.70	**61%**	0.980	**1.780**
OMW	0.45		0.621	
PTFE bearings	-		0.136	**87%**
Supporting ribs	-		0.040	
Pinion	-	-	0.003	
Rack	-	-	0.043	**0.270**
DC motor			0.096	
DC motor controller	-	-	0.009	**13%**
Feedback potentiometer	-	-	0.023	
Cabling	-	-	0.096	
Total	1.15		2.047	100%

The mass of the actuation mechanism is 0.270 kg which represents 13 % of the total mass. On the other hand, the structural components represent 87 % of the total telescopic wing-box mass, which is approximately 1.8 kg.

3.1.6. Wing-box preliminary structural sizing

This section presents the results of the preliminary sizing of the wing-box structure subject to the bending and torsion loads resulting from the aerodynamic loads of the four main design conditions considered in the project: take-off, loiter, high-speed and landing. The aim of this design is to produce a wing-box that provides the necessary strength and stiffness for all mission phases, within the bounds of the morphing specification. A simplified (conservative) lift distribution is used for this preliminary sizing.

The preliminary wing-box sizing is performed based on the loads shown in Table 3.3. It is assumed that the wing-box alone takes all loads resulting from the aerodynamic forces and moments. By doing this, no contribution from the skin of the wing is considered. Other loads,

such as structure and systems' weight and any contributions from actuators, are not taken into consideration at this stage. However, the weight of the wing-box itself is considered. Assuming that the shape of the distribution is not affected by the angle of attack and the drag, and pitching moment distributions are uniform along the wing span, the lift distributions along the wing span were obtained with a polynomial approximation. The latter subject is better described later in section 4.2.

Since the wing operates at different angles of attack, the lift and drag force are rotated to produce a vertical force perpendicular to the wing chord and a horizontal force parallel to the wing chord. The distributions of these forces along the span are represented in Figure 3.14, Figure 3.15, Figure 3.16 and Figure 3.17.

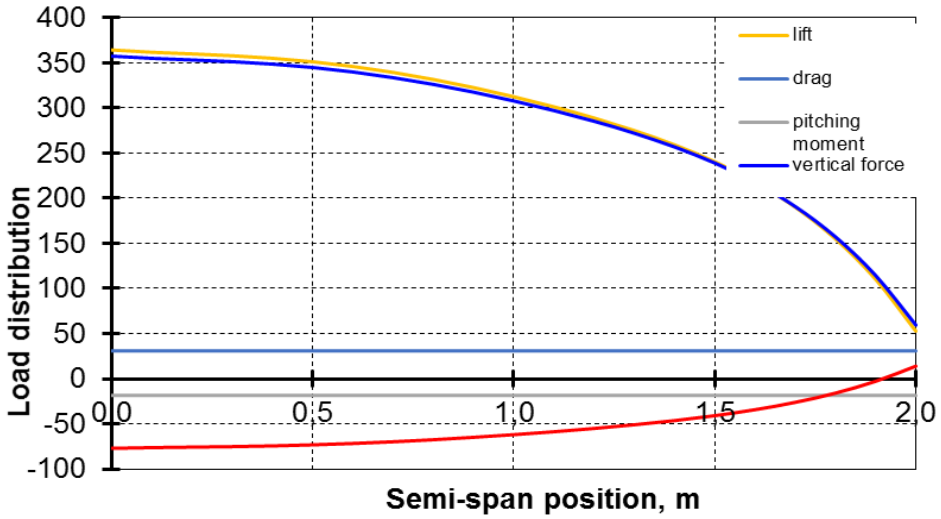

Figure 3.14: Load distributions for loiter wing configuration at low speed

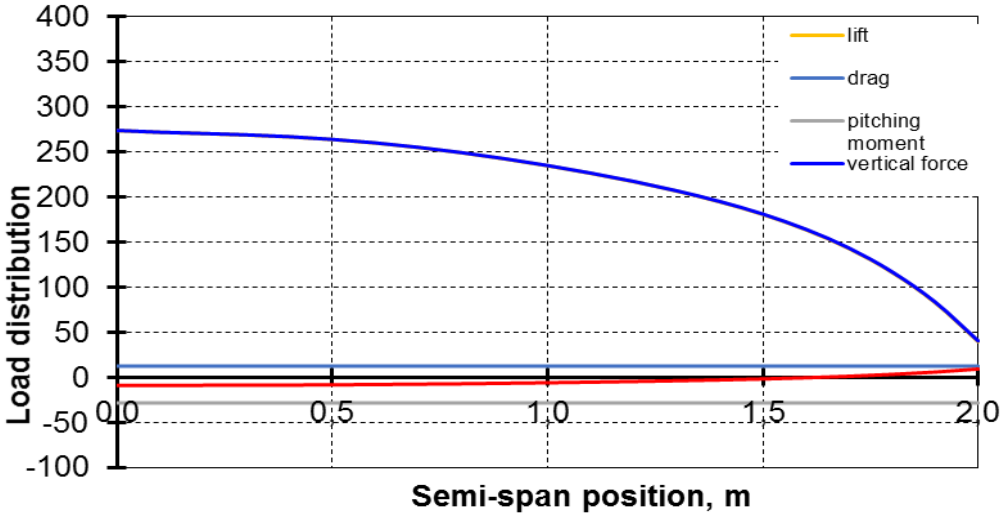

Figure 3.15: Load distributions for loiter wing configuration at high speed

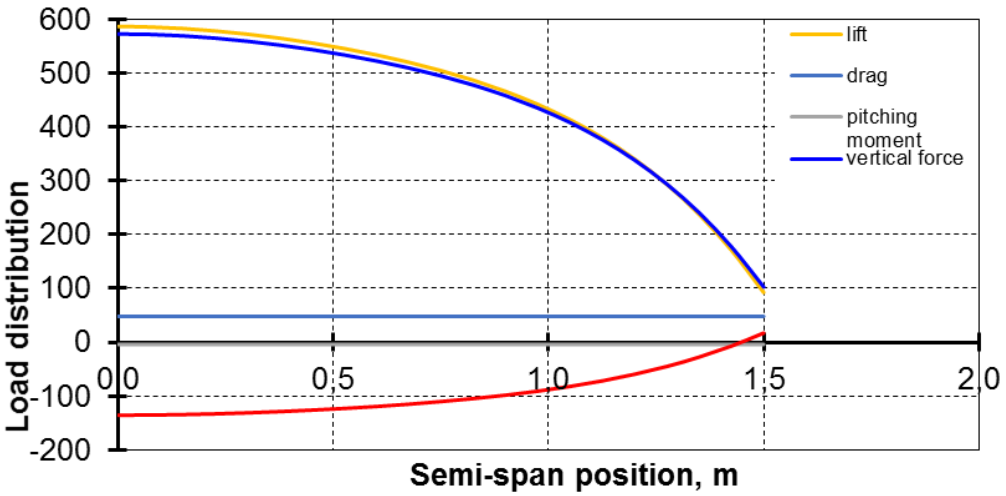

Figure 3.16: Load distributions for high-speed wing configuration at low speed

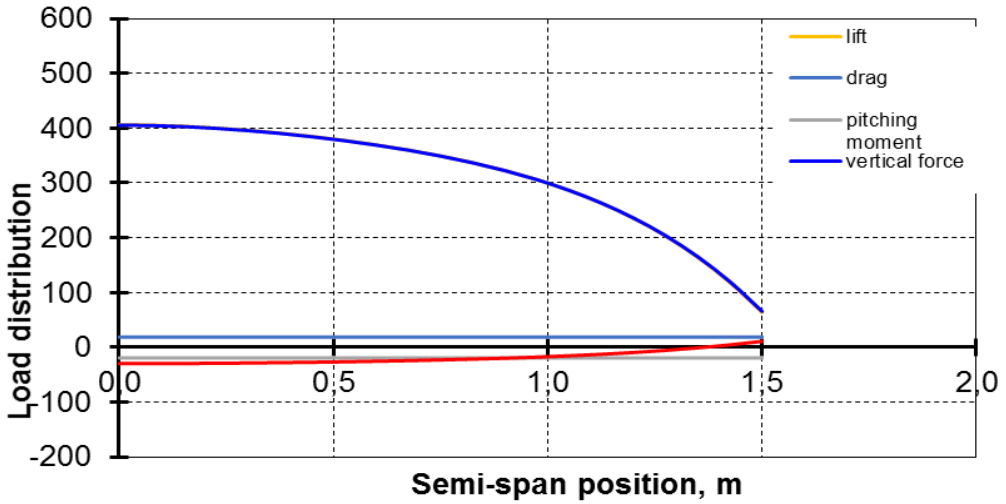

Figure 3.17: Load distributions for high-speed wing configuration at high speed

In order to better represent the load distributions along the chord, the initial force system of one vertical force, one horizontal force applied at 25 % of the wing chord and a torsion moment about this point is substituted by two vertical forces applied at the fore and aft wing-box webs and four horizontal forces applied at each spar cap, as shown in Figure 3.18.

The equivalent force system in this case is presented in Table 3.8. The fore vertical load is distributed along the front of the wing-box, the aft vertical force is distributed along the rear of the wing-box and the horizontal force is equally distributed by the four spar caps. The equivalent force distributions are calculated from the load distributions multiplied by the safety factor.

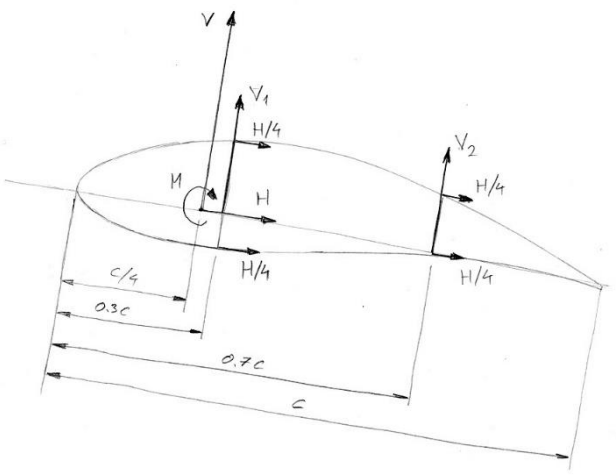

Figure 3.18: Equivalent force system for wing-box sizing (V is the vertical force, H the horizontal force and M the pitching moment)

Table 3.8: Equivalent loads

	Loiter		High-speed	
	Low speed	**High speed**	**Low speed**	**High speed**
Fore vertical load [N]	1012	413	1689	882
Aft vertical load [N]	674	871	330	540
Horizontal load [N]	-322	-26.5	-429	-85.4

The following analyses of the wing-box for the four design conditions - extended wing at low speed; extended wing at high speed, retracted wing at low speed and retracted wing at high speed – were performed using ANSYS Structural APDL. The objective of the structural sizing is to minimize the weight of the wing-box, subject to a maximum tip deflection of 0.05 m, a maximum twist angle of the tip chord of 5 degrees, maintaining all stresses below the ultimate stresses of the materials and the inverse of Tsai-Wu strength ratio[7] below 1 to avoid failure. It is also assumed that the thickness of a single carbon/epoxy layer is 0.12 mm.

[7] ANSYS® Academic Research, Release 14.5, Mechanical APDL Theory Reference, Chapter 9, ANSYS, Inc. 2011.

- Extended wing configuration – low speed

This condition corresponds to the wing configuration for loiter at 80 km/h.

Figure 3.19 shows the total displacement of the wing-box in the loiter configuration. It is possible to see a smooth deformation increasing from root to tip, reaching a maximum of 0.04 m. The tip displacement is relatively low (only 1 % of the span) but necessary to allow an even slide of the two wing components. In fact, if the tip displacement had much higher values, the wing-box mechanism could jam, compromising system integrity and functioning.

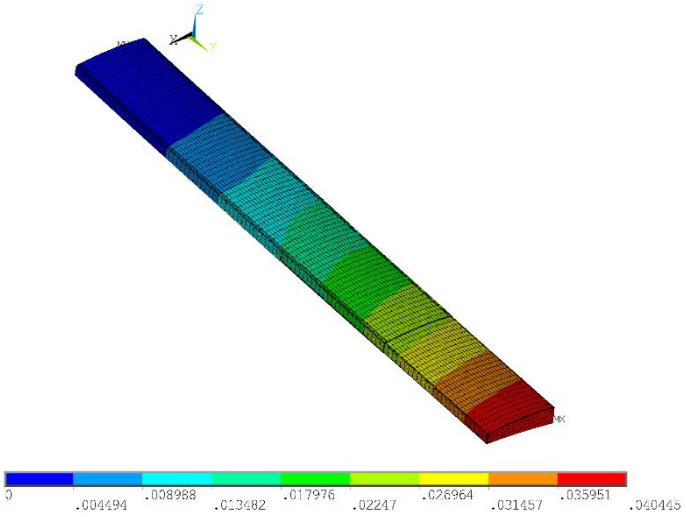

Figure 3.19: Total displacement of the loiter wing in the low speed condition

In Figure 3.20 the inverse of Tsai-Wu strength ratio criteria of the two sections of the wing-box for each layer is shown. Regarding the IFW (a) to c)), it is possible to conclude that the wing-box is slightly oversized since the Failure Criteria (FC) never exceeds 0.32. As expected the more stressed areas are located near the end of the wing-box web, since this region is supporting the outboard moving portion. The generalized lightly loaded structure results from the fact that the minimum thickness allowed in the composite laminate is 0.12 mm.

Now regarding the OMW (d) to f)), very similar conclusions can be drawn out. Again the more stressed areas are in the contact region between the two wing elements. The maximum Failure Criteria is 1.12 in a small localized area in the outer carbon-epoxy layer near the root of the OMW (smaller than 2 mm^2).

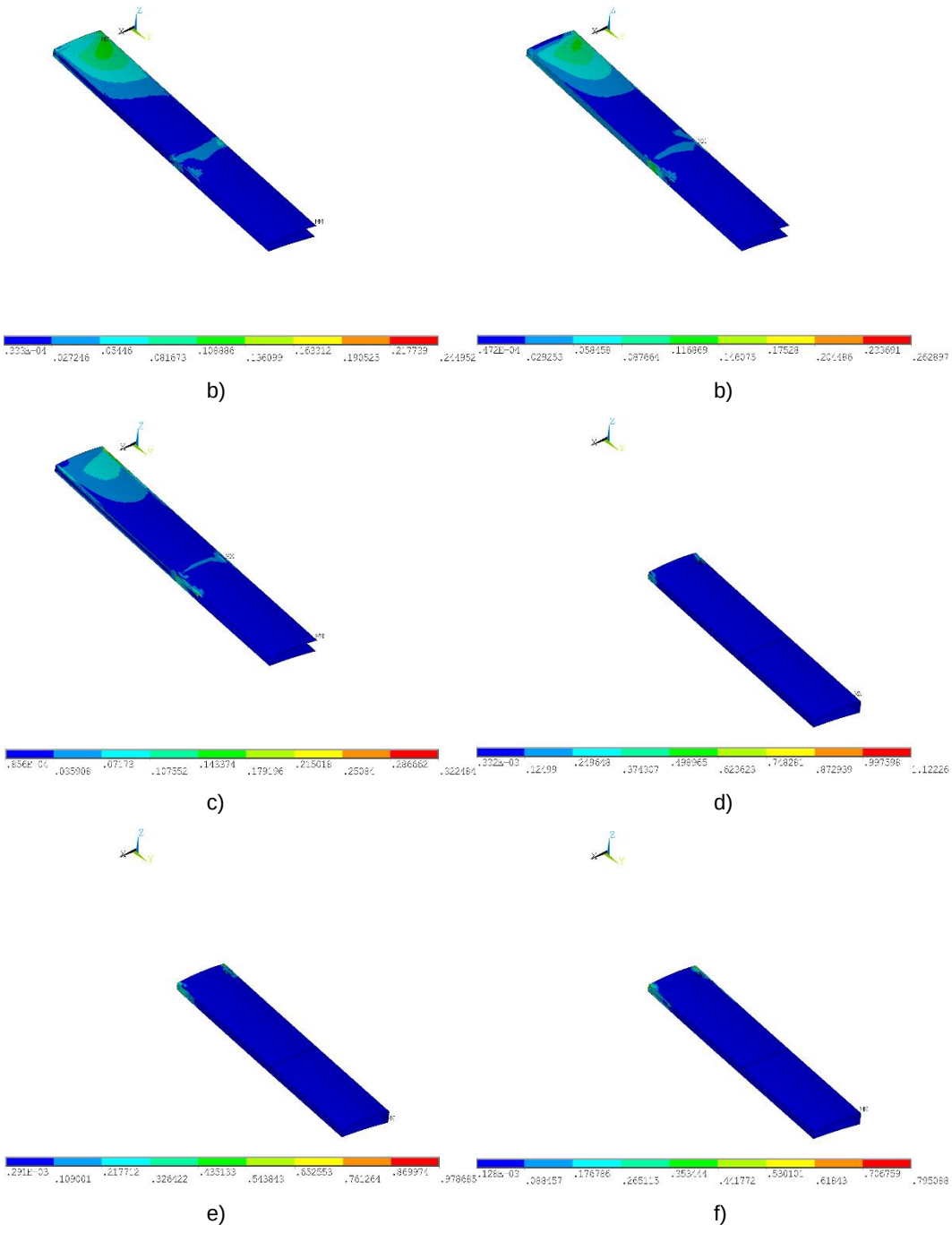

Figure 3.20: Inverse of Tsai-Wu strength ratio of the two main bodies that constitute the wing-box: a), b) and c) show the three layers of the inboard fixed portion and d), e) and f) the three layers of the outboard moving portion

- Extended wing configuration – high speed

This condition corresponds to the configuration of the loiter wing at 95 km/h. The configuration is the same as in the previous case, only the speed and the load factor differ.

Figure 21 shows the total displacement of the wing-box. It is possible to see the deformation increasing from root to tip as in the previous case. The tip displacement is inferior to the low speed loiter case, being the maximum value 0.031 m (a 25 % reduction).

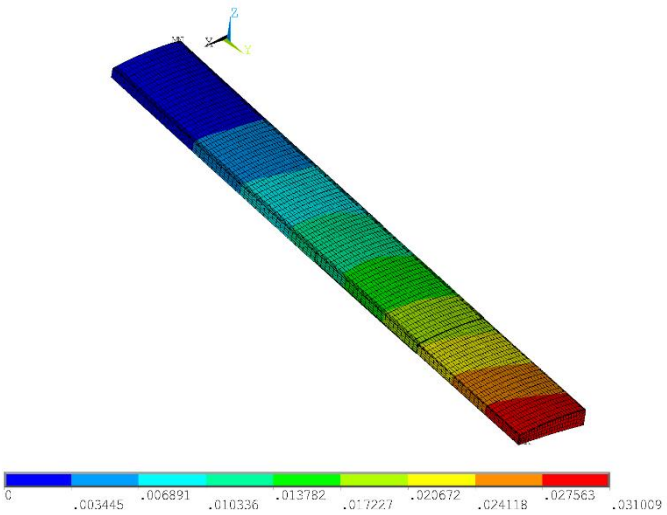

Figure 3.21: Total displacement of the loiter wing in the high speed condition

The inverse of Tsai-Wu strength ratio criteria for the two sections of the wing-box and for each layer is shown in Figure 3.22. Observing the fixed portion of the wing-box (a) to c)), the more stressed areas are located near the end of the wing-box web, as in the previous case. However, the Failure Criteria is now lower than the previous case and does not exceed 0.25.

Regarding the moving portion of the wing-box (d) to f)), very similar conclusions can be drawn out. Again the more stressed areas are in the contact region between the two wing elements. Unlike the previous case study, the maximum Failure Criteria never exceeds the unity, being about 0.85 in the outer carbon-epoxy layer at the root of the OMW.

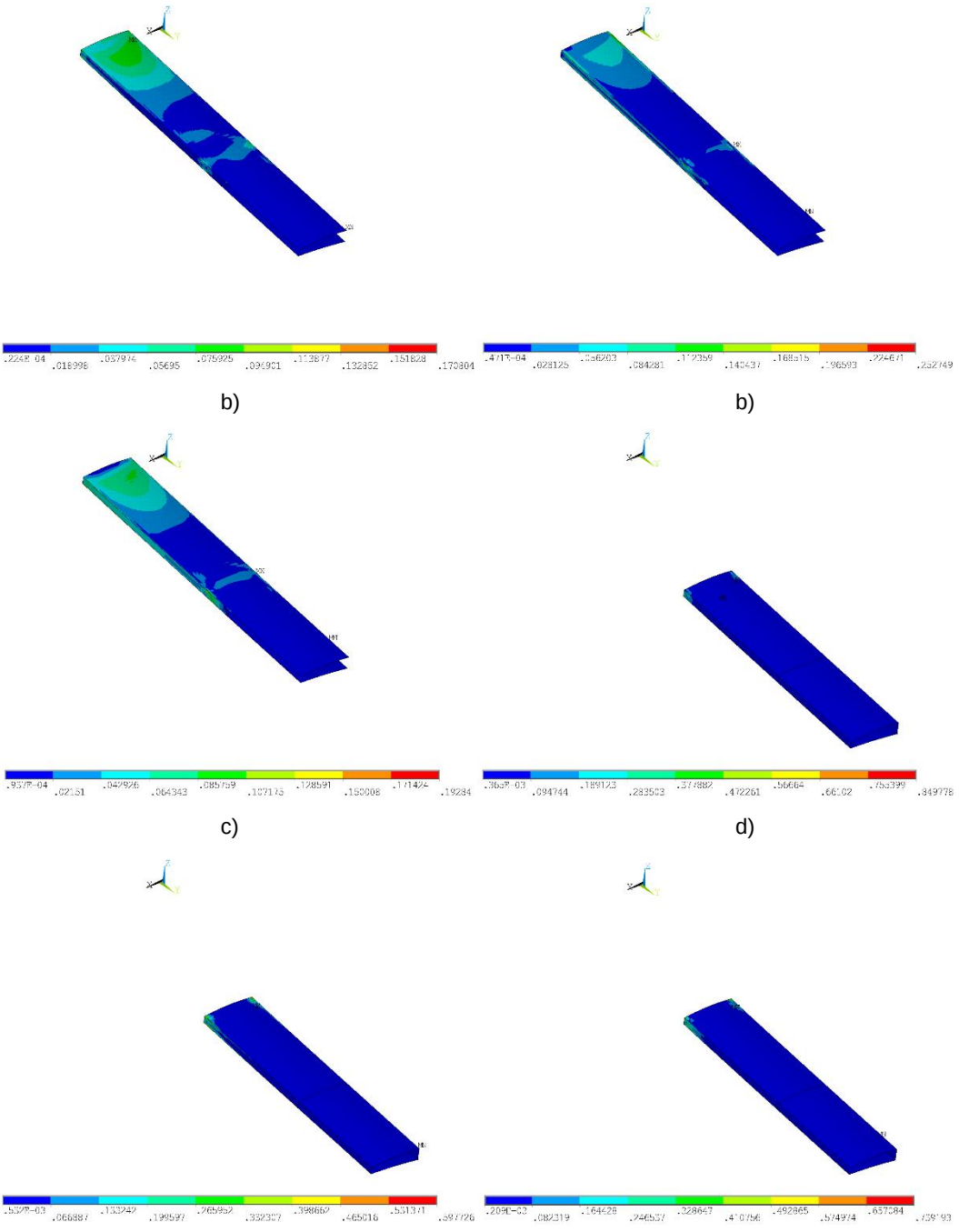

Figure 3.22: Inverse of Tsai-Wu strength ratio criteria of the two main bodies that constitute the wing-box: a), b) and c) show the three layers of the inboard fixed portion and d), e) and f) the three layers of the outboard moving portion

- Retracted wing configuration – low speed

This condition corresponds to the high-speed wing configuration at 110 km/h.

Figure 3.23 shows the total displacement of the high speed wing in the low speed condition of the wing-box. Similar conclusions can be drawn out such as an increase deformation from root to tip. The tip displacement is inferior to both loiter conditions, being the maximum about 0.028 m. The maximum twist angle appears at the wing tip and has a value of 0.6 degrees.

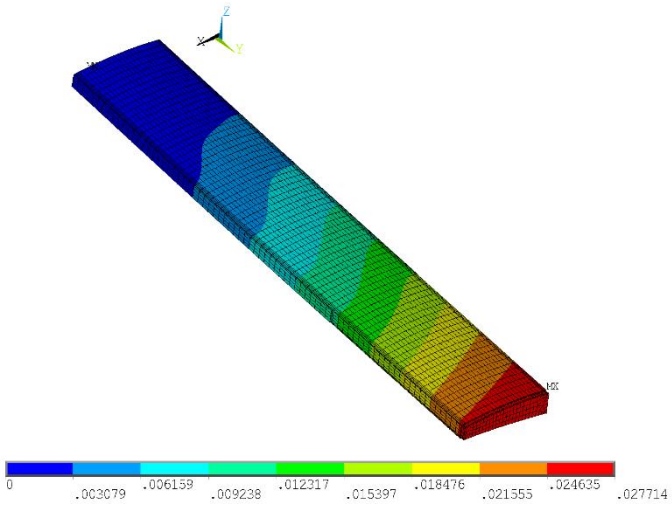

Figure 3.23: Total displacement of the high speed wing in the low speed condition

In Figure 3.24 the inverse of Tsai-Wu strength ratio criteria is shown. Observing the fixed portion of the wing-box (a) to c)), it is immediately visible that unlike in the configuration for loiter, the stress concentration near the end of the wing-box web disappeared. This is due to the fact that the OMW is fully retracted. Therefore the area that supports the load is greatly increased and the bending moments are reduced due to the reduced wing span.

Regarding the OMW (d) to f)), one can conclude that the loading is mainly transferred through the IFW and because of this the loading in the former component is greatly reduced. However, when under load, the IFW reduces its section by a small percentage and that causes a squishing effect on the OMW.

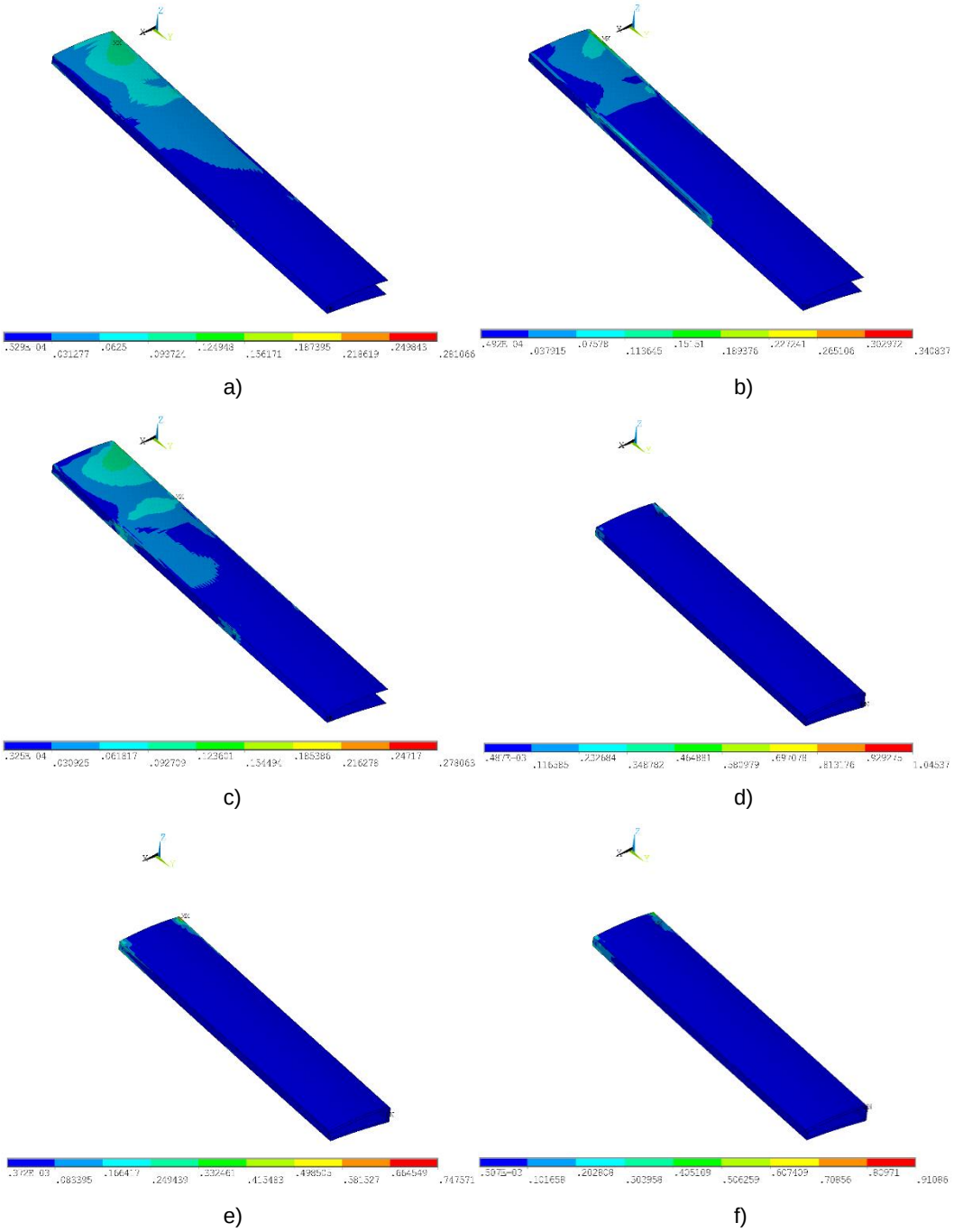

Figure 3.24: Inverse of Tsai-Wu strength ratio Failure Criteria of the two main bodies that constitute the retracted wing-box at the lower speed condition: a), b) and c) show the three layers of IFW and d), e) and f) the three layers of the OMW

- Retracted wing configuration – high speed

This condition corresponds to the high-speed wing configuration at 138 km/h.

Figure 3.25 shows the total displacement of the wing-box. Again, it is possible to see a deformation that grows from root to tip. The tip displacement is the smallest of all studied conditions, being about 0.019 m. The maximum twist angle takes place at the wing tip with a value of 0.16 degrees.

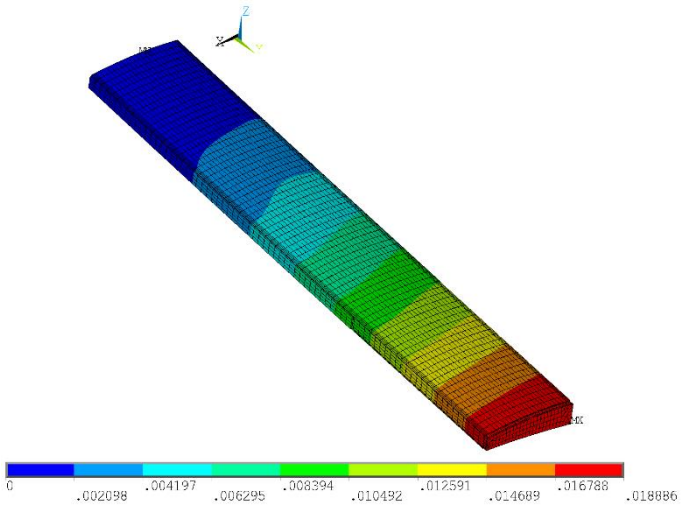

Figure 3.25: Total displacement of the high speed wing in the high speed condition

Figure 3.26 shows the inverse of Tsai-Wu strength ratio criteria of the IFW and OMW. The situation is very similar to the former condition: the stress concentration near the end of the wing-box web disappeared.

Concerning the OMW (d) to f)), we can see that the Tsai-Wu Failure Criteria is well below unity, being the maximum value 0.72.

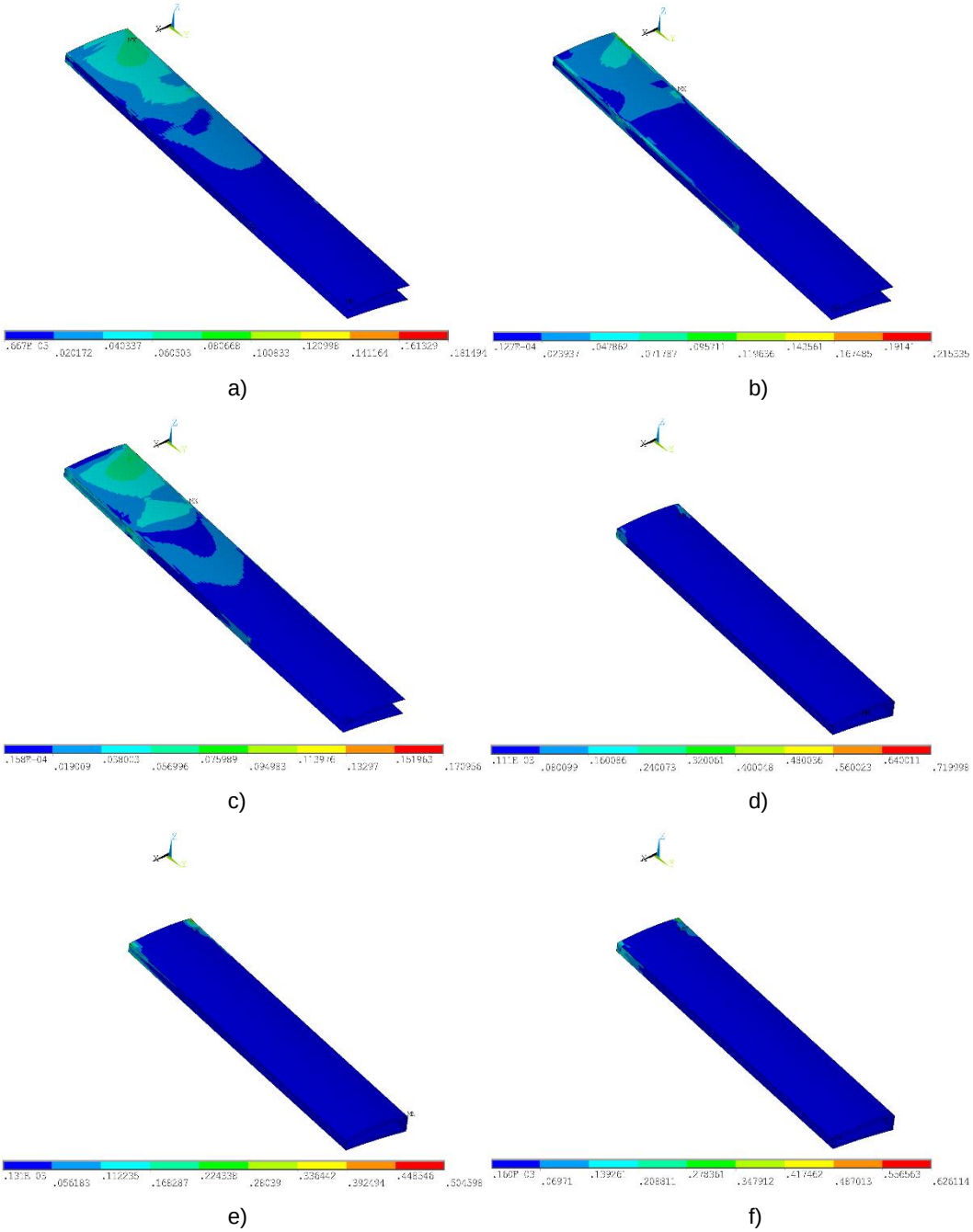

Figure 3.26: Inverse of Tsai-Wu strength ratio criteria of the two main bodies that constitute the retracted wing-box in the higher speed condition: a), b) and c) show the three layers of IFW and d), e) and f) the three layers of the OMW

4. Parametric study of the wing-box

The need of this study is to provide other partners with analytical functions to include in the morphing assessment software of the CHANGE Project. The software will be capable to provide the best wing shape and to fly with the highest performance possible for any given morphing wing. The user shall provide, as an input to the software, the actuator locations and limitations, as well as the mission(s) assigned to the aircraft. The outcome of the software will be the desired wing shape and actuator settings that the wing must endure in order to fly the mission with the best performance possible. Therefore a correct model of the wing´s mass is important for the correct estimate of the wing size and configuration.

The structural analysis in this work is divided into two parts. First, using the telescopic wing structural analysis model developed in the research group by Pedro Santos, estimates of the mass of the preliminary wing design were made. After a brief understanding of how the mass varied with wing's span moving fraction, a few changes were made to the numerical model previously cited in order to refine the analysis and collect more data with respect to the mass variation and displacement of the wing according to different moving fractions and wing span, which was the main objective of this work. In the second part, experimental tests were made to the prototype built to validate and confirm the theoretical study.

4.1. Numerical model

The model's initial purpose was to analyse the Olharapo's wing for different flight conditions [39] and was adapted to assist the structural analysis of this work. This subsection describes the structural analysis model and the modifications made to it.

The first step for building the Finite Element (FE) model is the generation of the geometry entities that will then be used for creating the mesh. The geometry does not have to be an accurate representation of the actual shape of the wing, but a useful intermediate step for the generation of the FE mesh. In this model's section, the wing's geometry was stated such as the dimensions described in section 3.1.5 which can be seen in Figure 3.12 and the materials described in section 3.1.3. As the changes that intended to carry out this study were geometric, the numerical model was mostly modified here so as to be as interactive and easy as possible to constantly modify the parameters and perform all the intended analysis to collect data. The modifications to the numerical model concern parameters such as the wing's semi-span and moving fraction. These are used mainly to obtain the mass and displacement at the wing tip.

The numerical model of the wing-box is developed in ANSYS Mechanical using the ANSYS APDL defined with shell elements according to the preliminary wing-box design. The original APDL script written was modified to handle distinct geometry changes, material definition, section properties and meshing.

SHELL181 elements were used to build the IFW as well as the OMW. The sandwich skins of the two wing's portions are modelled with three layers built as offset surfaces from the airfoil contour according to its own thickness. These three layers constitute the carbon epoxy and PVC sandwich. In the locations of the embedded spar, the PVC foam layer is replaced with unidirectional pultruded carbon-epoxy. The SHELL181 element is suitable for analysing thin to moderately-thick shell structures. It is a four-node element with six degrees of freedom at each node: translations in the *x*, *y*, and *z* directions, and rotations about the *x*, *y*, and *z*-axes. This type of element is well-suited for linear, large rotation, and/or large strain nonlinear applications. Additionally, the change in shell thickness is taken into account in nonlinear analyses.

The wing's structure required the use of contact elements between the IFW and OMV. The contact takes place in the overlap surface between the two portions of the wing and is modelled with a shell to shell contact using TARGE170 (target element for 3D geometries) and CONTA173 (contact element for 3D shells without mid side nodes). Then, two sets of contact pairs between the contacting surfaces are generated. Boundary conditions are defined as a few constraints, settled by CONTA and TARGE elements, such as the interaction between the IFW and the OMW or the gap between these. The interface between the inboard fixed portion and the outboard moving portion is modelled by a symmetric contact pair using contact elements. This was chosen over a rigid connection to enhance the FE model fidelity.

The FE model is considered to be built-in in the vicinity of the wing-box root. Additionally, the outboard moving component is constrained in the *y*-direction to simulate the actuator connection.

Figure 4.1 shows the complete assembled finite element model and the different assemblies that compose the FE model.

The first outcome of the model is the wing-box's mass. The final solution that can be seen in the model is the static analysis of the wing-box according to the loads that the wing is subjected. All loads are multiplied by a safety factor of 1.5. Figure 4.2 shows an example of the final solution representing the displacement for a semi-span of 2 m and a moving fraction of 0.25.

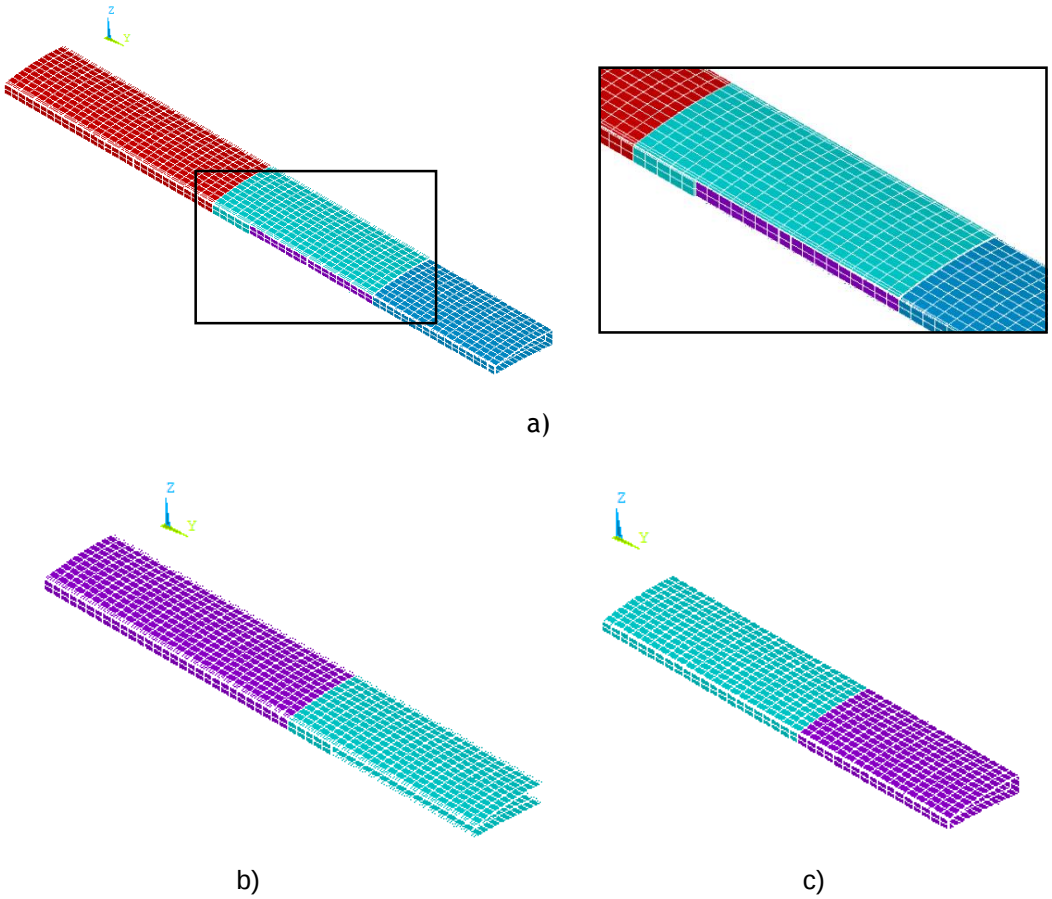

Figure 4.1: Variable-span wing model in ANSYS Mechanical APDL: a) complete finite element model and a detail of the interface between the IFW and OMW, b) IFW layered shell and c) OMW shell

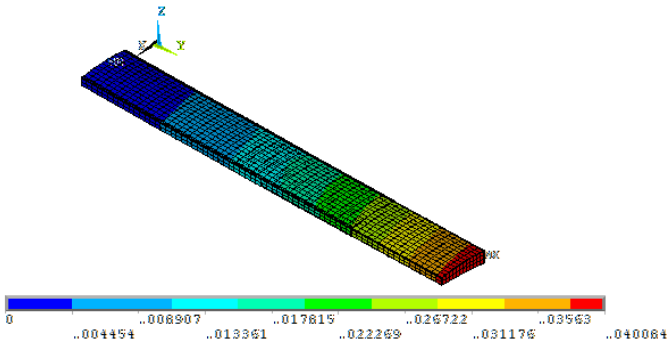

Figure 4.2: Numerical model's example of final solution (displacement)

For a steady state simulation we need to ensure that the solution satisfies domain balances of less than 1 % so a convergence analysis of the finite element model was carried out to assess the sensitivity of the maximum tip deflection as a function of the number of elements in the grid. During this study, a rigid contact between the IFW and OMW was considered. The refinement of the grid mesh was done by changing the default element size of the original script. Figure 4.3 shows the convergence of the maximum wing tip deflection for several mesh sizes. It is possible to conclude that the solution stabilized around 77300 elements but for practical

reasons the number of elements used was around 6300 elements which surely satisfies domain balances of less than 1 %, being 0.84 % for this number of elements.

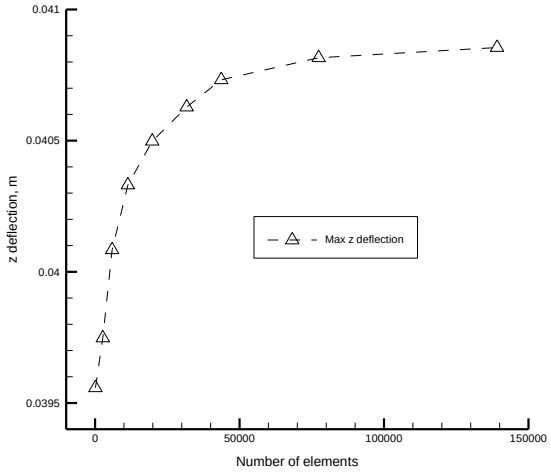

Figure 4.3: Maximum tip deflection obtained using different number of elements

4.2. Mass parametric study

The wing-box mass is highly dependent on the span of the wing and the amount of telescopic retraction required. For that reason, and in order to provide an insight into its dependence on these two parameters, a parametric study was conducted. The aim of this parametric study was to obtain two equations that express the wing-box mass and wing tip displacement, respectively, as functions of the wing span and the fraction of designed telescopic motion of the OMW. Polynomial approximations were used to represent these functions. In the analysis, the wing-box cross section size is kept unaltered.

Structural mass estimation

The parameters used in the study are as follows:

m = Wing-box total mass [kg]

p = Moving fraction (maximum span variation divided by maximum span)

b = Wing span [m]

δ *= Wing tip displacement [m]*

FC = Failure Criteria

θ *= Twist angle [°]*

In this study, all displacements presented were calculated with the wing-box fully extended for wing spans of 2 m, 2.5 m and 3 m and percentage of telescopic motion between 5 % and 30 %.

Two other modifications were also made to the wing-box design in order to refine the analysis and collect more data. Firstly, one of the IFW carbon fibre webs' layers was removed so that the carbon fibre thickness was reduced from 0.24 mm to 0.12 mm (this case is called Case B). Secondly, one of the IFW webs' two carbon fibre layers was removed and the foam cores' thicknesses were reduced by 1 mm, from 3 mm to 2 mm (this case is called Case C). Both modifications are shown in Figure 4.4 and are highlighted with red circles. The originally designed cross-section structure (described at Section 3.1) is called Case A.

As described in the wing-box preliminary structural sizing, and in order to better represent the load distributions along the chord, the initial force system of one vertical force and one horizontal force, both applied at 25 % of the wing chord, and a torsion moment about this point is substituted by two vertical forces applied at the fore and aft wing-box webs and four horizontal forces applied at each spar cap. When the fully extended span of the wing is changed, the total lift is kept constant but it is distributed over the new span.

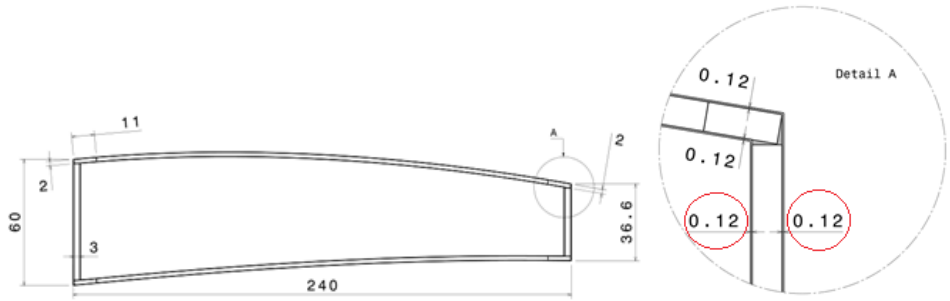

Case B)

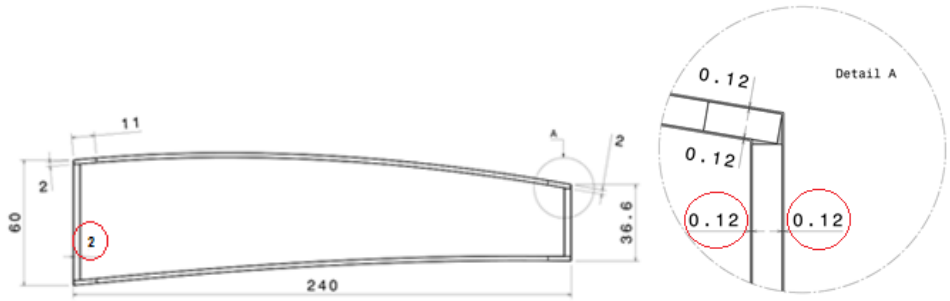

Case C)

Figure 4.4: Preliminary wing-box design modifications to support the study: Case B) webs' laminate thickness reduction and Case C) webs' laminate and core thicknesses reduction

The wing-box total mass, wingtip displacement, maximum twist angle of the tip chord and the Failure Criteria are performed using ANSYS Structural APDL. The wing-box analysis corresponds only to one wing's structure.

Figure 4.5 summarizes the values for the preliminary wing-box design, having a semi-span of 2 m. On the left graph, the curves represented are: a) preliminary (Case A) wing-box mass, b) preliminary (Case A) wing-box displacement, c) wing-box mass of Case B, d) wing-box tip displacement of Case B, e) wing-box mass of Case C, and f) wing-box tip displacement of Case

C. On the right graph, the curves represented are: f) wing-box tip displacement of Case B, and d) wing-box tip displacement of Case C.

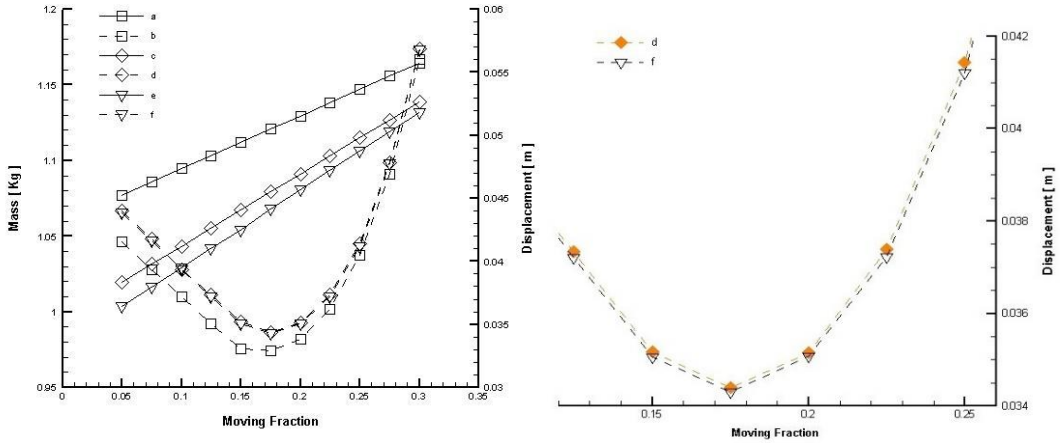

a) b)

Figure 4.5: ANSYS' wing-box mass and displacement as functions of moving fraction for a semi-span of 2 m: a) values given for moving fraction between 0.05 and 0.3; and b) detail of displacement curves

As shown in the graphs above, with the reduction of one carbon fibre layer in the webs and after the reduction of 1 mm of the web core thickness, the wing-box total mass reduces and the wing tip displacement increases about 4 %. Although it is not very noticeable, the wing tip displacement of the wing-box of Case B is slightly smaller than the wing tip displacement of the wing-box of Case C. The Failure Criteria and the wing tip deflection in all cases never exceeded 0.57 and 0.06 m, respectively.

Figure 4.6 shows the results of the study for the modifications described earlier but for the 2.5 m and 3 m semi-span wings. The mass and displacement trends are similar to those of the 2 m semi-span but the values are slightly increased.

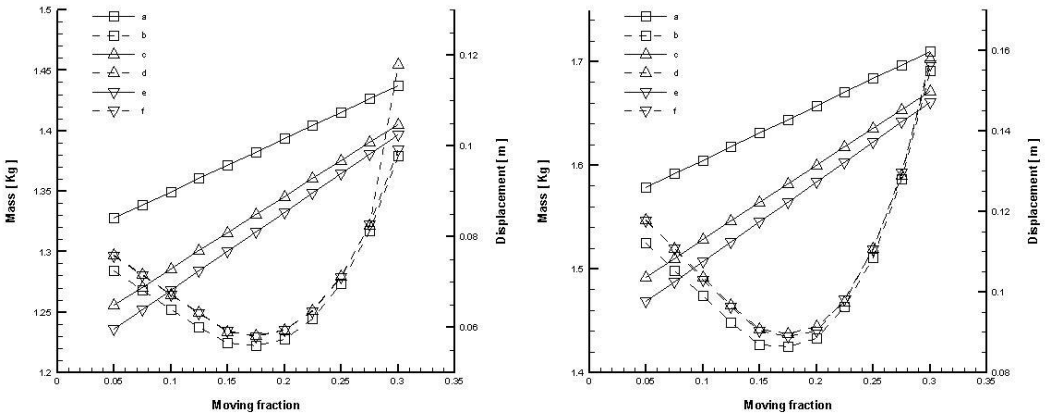

Figure 4.6: ANSYS' mass and displacement analyses: a) semi-span of 2.5 m; and b) semi-span of 3 m

In Table 4.1, three cases of the mass variation according to the wing-box's design described in Section 3.1 are shown, each with distinct moving fraction and/or wing span. Also, the wing tip displacement, Failure Criteria and wing twist are presented.

Table 4.1: Main results of parametric analysis for the original cross-section (Case A)

Semi-span [m]	Moving fraction	Mass [kg]	Displacement [m]	Failure Criteria	Twist [°]
2.0	0.05	1.077	0.0416	0.311	0.0438
2.0	0.20	1.130	0.0338	0.347	0.0600
2.0	0.30	1.165	0.0560	0.335	0.0803
2.5	0.05	1.328	0.0724	0.391	0.0568
2.5	0.20	1.393	0.0573	0.452	0.0833
2.5	0.30	1.437	0.0977	0.435	0.1110
3.0	0.05	1.579	0.1122	0.465	0.0677
3.0	0.20	1.657	0.0885	0.558	0.1029
3.0	0.30	1.710	0.1549	0.564	0.1430

Figure 4.7, Figure 4.8 and Figure 4.9 show the FE results of wing tip displacement, Failure Criteria and wing tip twist for the semi-span values of 2 m, 2.5 m and 3 m, and moving fraction values of 5 %, 20 % and 30 %, respectively (also for Case A).

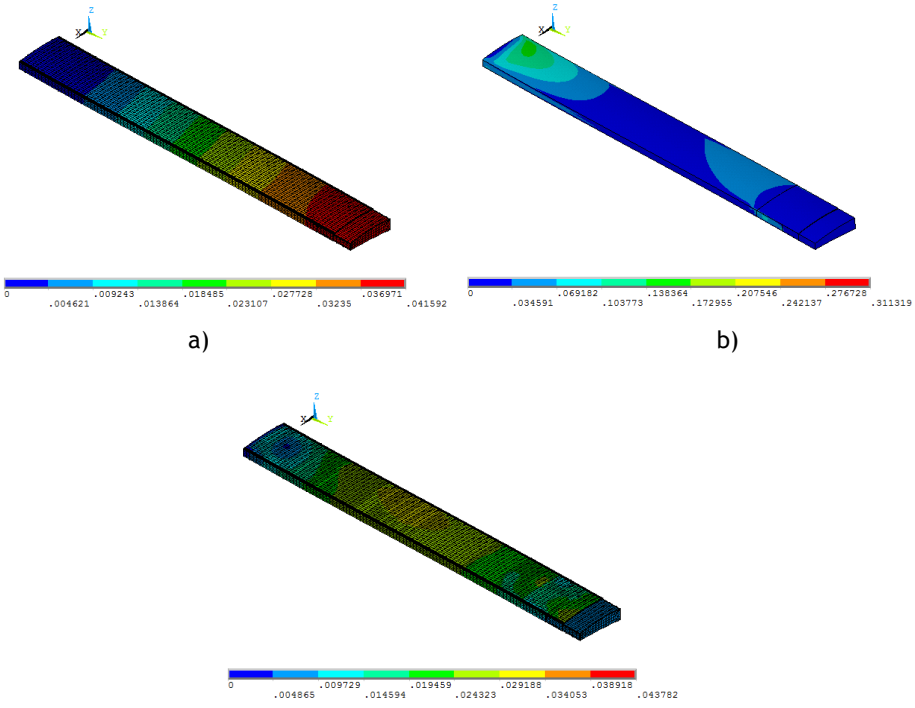

a) b)

-c)

Figure 4.7: ANSYS data for 2 m wingspan and 5 % moving fraction: a) wing tip displacement, b) Failure Criteria and c) wing tip twist (Case A)

In Figure 4.7 it can be seen a small deformation (displacement), as previously documented in Section 3.1, increasing from root to tip reaching a maximum value of almost 0.042 m. The Failure criteria is, approximately, 0.31 and, as concluded before, the wing-box is slightly over-sized. The maximum twist angle appears at the wing tip and is relatively small, being less than 1 degree. This indicates that the wing-box has torsional stiffness, which will facilitate leading and trailing edges morphing mechanisms integration.

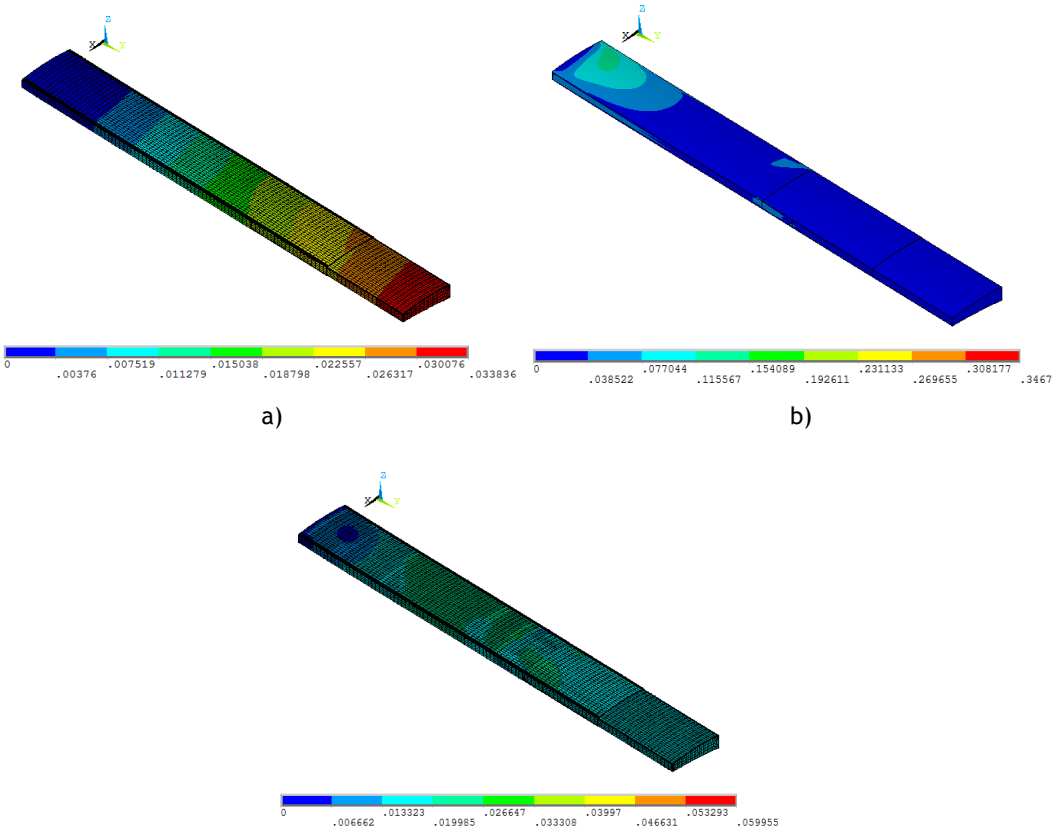

a) b)

c)

Figure 4.8: ANSYS data for 2 m wingspan and 20 % moving fraction: a) wing tip displacement, b) Failure Criteria and c) wing tip twist (Case A)

Regarding Figure 4.8, similar results and conclusions can be drawn out. The total displacement reaches a maximum value of, approximately, 0.034 m which is lower than the previous and can be explained by the proximity of the optimal value of the ratio between the moving fraction and the semi-span. The Failure Criteria is, approximately, 0.35 so the conclusions earlier made are suitable for this case. The maximum twist angle appears at the wing tip, as expected, being, also, less than 1 degree.

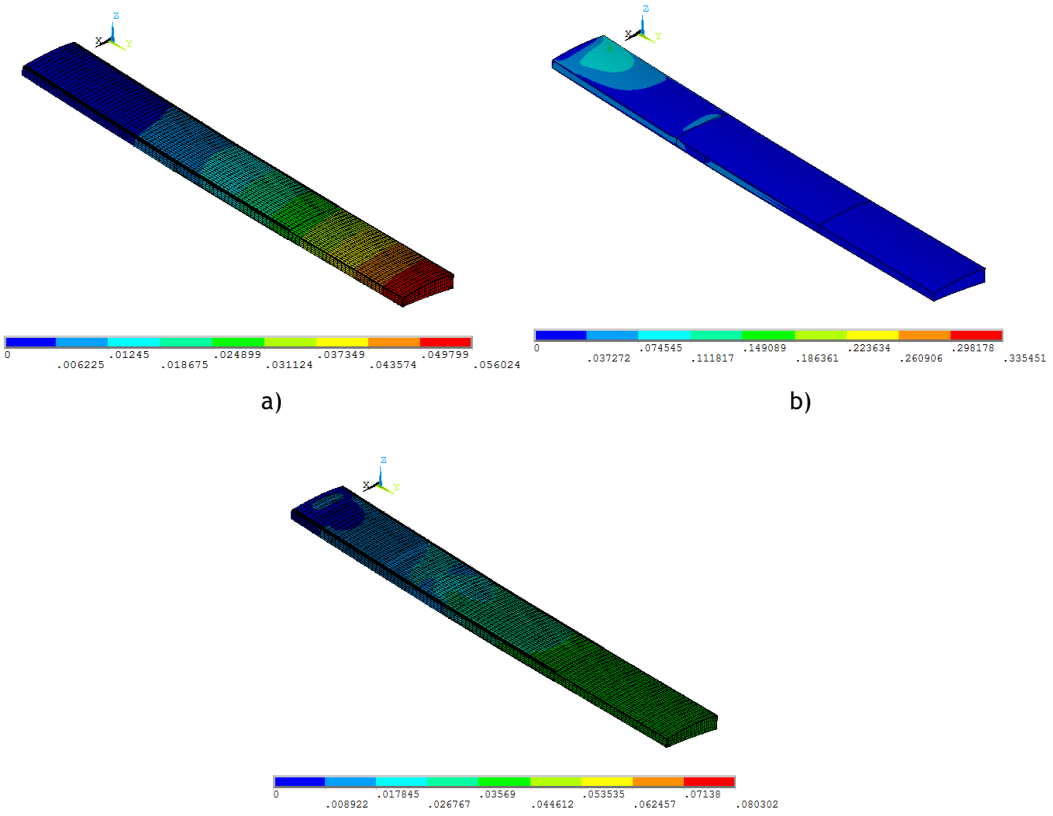

a) b)

c)

Figure 4.9: ANSYS data for 2 m wingspan and 30 % moving fraction: a) wing tip displacement, b) Failure Criteria and c) wing tip twist

As predicted, the wing-box's displacement and twist angle increases as the moving fraction is increased reaching maximum values of, approximately, 0.056 m and 0.08 degrees (with respect to a moving fraction of 30 % - Figure 4.9), respectively. Regarding the Failure Criteria, and as concluded in Section 3.1, due to minimum laminate thickness possible, it is seen that the wing-box is oversized as its value never exceeds 0.35 The more stressed areas are located near the tip of the IFW wing-box web, since this region is supporting the outboard moving portion.

In Appendix A.2 all the numerical values collected from the analysis are presented in tables A.1, A.2 and A.3.

4.2.1. Analytical representation

The results of the wing-box's mass and tip displacement are used to derive analytical expressions for the wing-box mass and tip displacement as functions of span and telescopic maximum moving fraction. These expressions are obtained by fitting a polynomial in two variables to the results shown in Figure 4.10 and Figure 4.11 for the original cross-section (Case A).

The polynomial equation that better expresses the mass variation is a second order polynomial of the form:

$$m\,(\,p\,,b\,) = 0.07402 + 0.4927\,p - 0.0001636\,\left(\frac{b}{2}\right) + 0.1752\,p\,\frac{b}{2} + \\ + 0.00001818\,p^2 + \,0.1752\,\left(\frac{b}{2}\right)^2 \tag{4.1}$$

Figure 4.10 represents this polynomial approximation corresponding to the wing-box's mass according to the design described in Section 3.1.

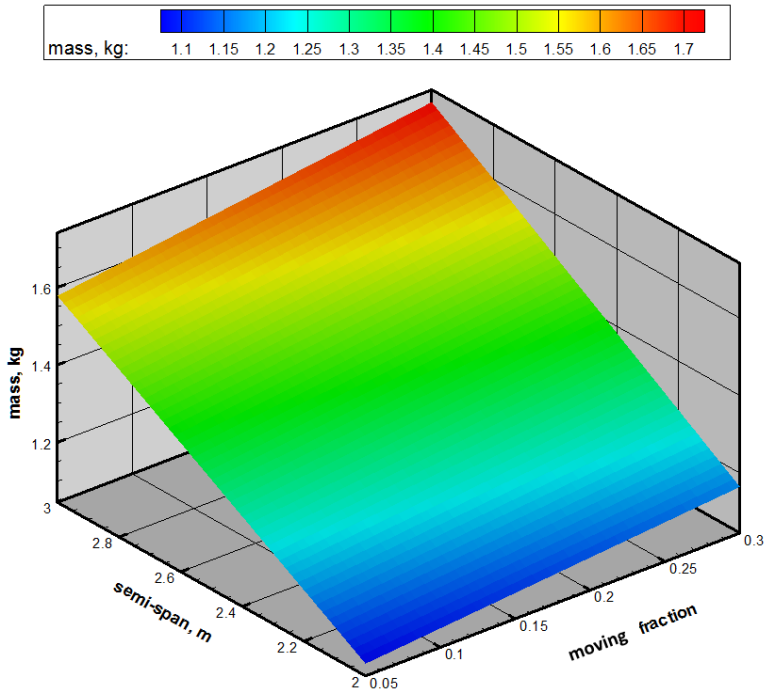

Figure 4.10: Polynomial approximation of wing-box's mass (Case A)

The generated equation that better expresses the wing tip displacement variation is a third order polynomial in the form:

$$\delta\,\,(\,p\,,b\,) = 0.04949 - 0.05638\,p - 0.9174\,\left(\frac{b}{2}\right) + 0.02668\,p^2 + 0.8259\,p\,\left(\frac{b}{2}\right) + \\ + 5.497\,\left(\frac{b}{2}\right)^2 - 0.1782\,p^2\,\left(\frac{b}{2}\right) - 4.734\,p\,\left(\frac{b}{2}\right)^2 - 7.247\,\left(\frac{b}{2}\right)^3 + \\ + 0.6266\,p^2\,\left(\frac{b}{2}\right)^2 + 6.875\,p\,\left(\frac{b}{2}\right)^3 - 4.672\,\left(\frac{b}{2}\right)^4 \tag{4.2}$$

Figure 4.11 represents this polynomial approximation corresponding to the wing-box's tip deflection according to the design described in Section 3.1.

Considering a semi-span of 2.00 m, the mass increases with increasing moving fractions. This happens because the overlapping of the IFW and OMW increases for larger moving fractions despite the decrease length of the IFW which is heavier when compared to the OMW. Figure 4.12 represents a graphical explanation of the previous description and helps to better understand this thought. Similar conclusions can be made for semi-spans of 2.50 m and 3.00 m.

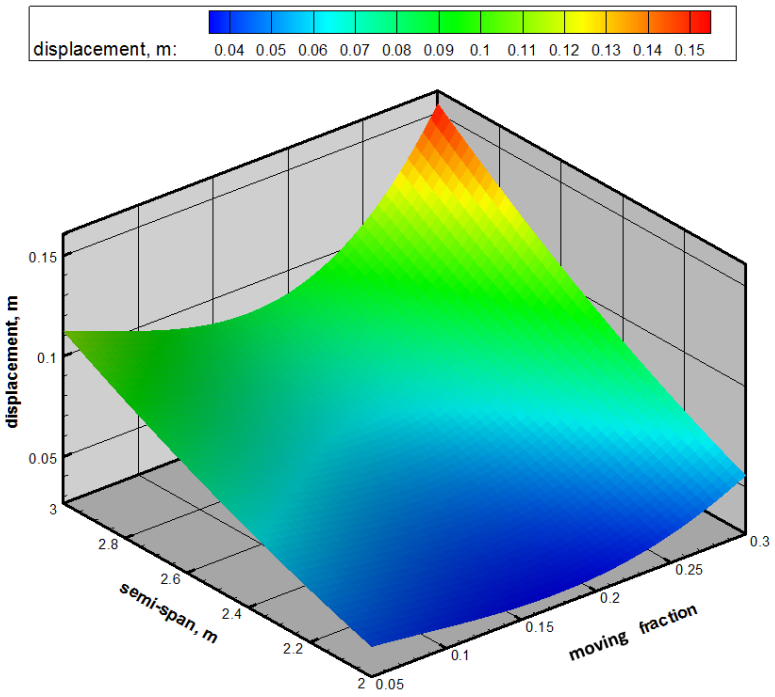

Figure 4.11: Polynomial approximation of wing-box's displacement (Case A)

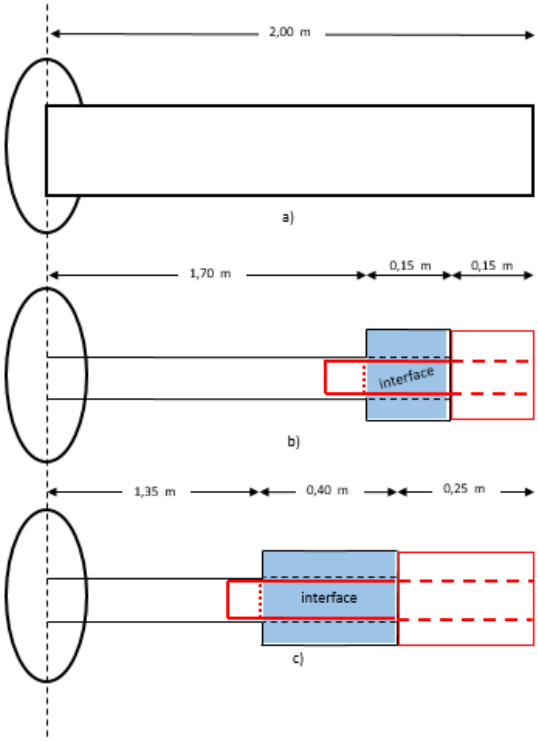

Figure 4.12: Interface variation according to different moving fractions: a) fixed wing, b) morphing wing with a moving fraction of 0.05, c) morphing wing with a moving fraction of 0.125

Regarding Figures 4.5 and 4.6 it can be seen that the curves present a minimum value of 0.033 m. This is due to the area where the moment is transmitted from the OMW to the IFW.

5. Wing-box testing

5.1. Test jig

5.1.1. Description and components

In order to ensure the system functionality under load, a static testing was performed in a jig specially developed for the current case. Before the construction was found that the structure would not suffer deflection during the experimental tests.

All the structure was built with rectangular tubes. Tube with size 30mmx20mm was used for the horizontal rails that allow the positioning of other components that can be added to the jig, which in this specific case, allow the placement of a 40mmx40mm size tube that houses the threaded rods through it and the load control nuts. Figure 5.1 shows the horizontal rails and the component tube added to perform the experimental setup which is placed in the top rails and can easily be moved through the rails by loosen two nuts and replace it. At the mid rails, a wooden board was placed, for practical reasons, to measure the displacements with a dial analogue comparator for the fore position and a graduated ruler for the aft position of the aerofoil. The two vertical tubes size 60mmx40mm at the middle of the structure were placed to prevent displacements of the rail tubes. The outer tubes (at both sides of the jig) are size 50mmx30mm and prevent the jig's buckling.

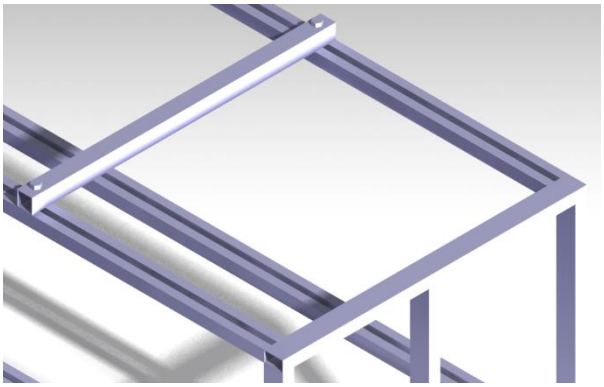

Figure 5.1: Horizontal rails and component tube

Figure 5.2 shows the jig's dimensions and the tube's distinct sizes.

The tension or compression control is performed with the load cells and the output of the data acquisition system. Figure 5.3 shows the load cells model [42] used at the experimental setup.

A dial analogue comparator and a graduated ruler were used to measure the displacements resultant from the fore and aft loads applied at the wing-box prototype. Figure 5.3 also shows the comparator and the ruler used in the experimental setup.

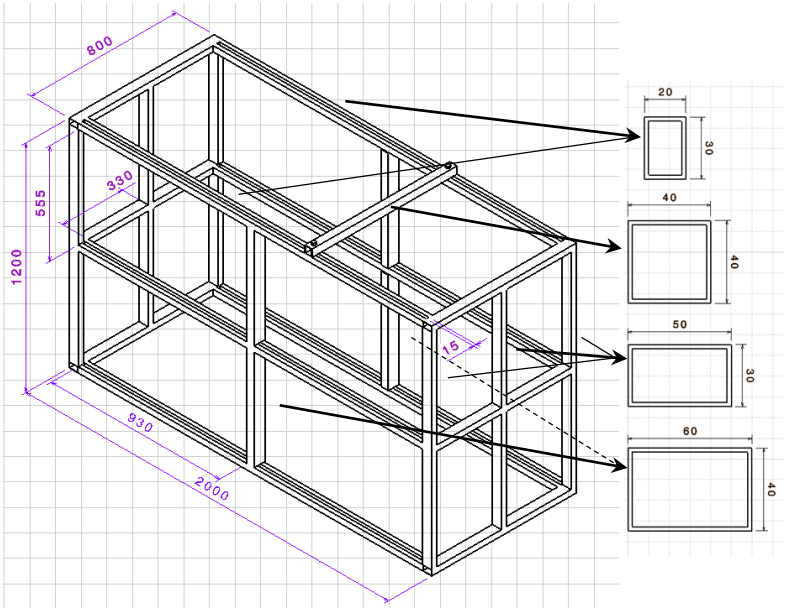

Figure 5.2: Jig's dimensions in mm

The load cells receive an excitation rate which is calibrated by the strain gage [43], a device whose electrical resistance varies in proportion to the amount of strain in the device. The PXI system of this device operates as a signal conditioning system for data acquisition devices. After the strain gage calibration and the signal testing using LabVIEW®[8] the applied forces are can be seen through the latter software. Figure 5.3 also shows the modular instrument used to collect data and apply the correct load.

a) b) c)

Figure 5.3: Components used for the experimental tests a) load cells, b) data acquisition system and c) graduated ruler and dial analogue comparator

A load transfer rib had to be placed for the correct load application to the prototype. Made from plywood, the load transfer rib was constituted by two glued laminates. For safety reasons a third and fourth smaller laminates were used at the extrados and intrados so the load transfer rib did not displaced from its original position. Figure 5.4 shows the load transfer rib placed in the wing-box prototype for the experimental setup.

8 Base software from National Instruments platform design. Retrieved from: http://www.ni.com/labview/pt, 02/10/2014

The loads are transferred to the prototype by two pairs of rod end bearings. Each pair is constituted by a rod end bearing [44] and a Studded rod end bearing [45]. Figure 5.4 also shows the two types of rod end bearings used in the experimental setup.

a) b) c)

Figure 5.4: Components used for the experimental tests a) load transfer rib, b) rod end bearings and c) studded rod end bearing

All the screws, nuts and rod end bearings used are M12.

5.2. Experimental setup

In Figure 5.5 it is possible to see the assembled test bench with the wing mounted.

Figure 5.5: Assembled test bench with the wing mounted

The loads are applied at the wing-box structure near the wing-box webs as can be seen in Figure 5.6. It can also be seen the load transfer rib, the two pairs of rod end bearings and the load cells.

Figure 5.6: Wing-box test bench assembly

The loading is increased or decreased by tightening the two nuts connected to the structure which force the threaded rods to move up or down. The applied loading is monitored using two

load cells and is transferred to the prototype by two pairs of rod end bearings. The rod end bearings avoid out of plane loads and allow the prototype to deform without constrains. In Figure 5.7 it is possible to see the main components of the jig.

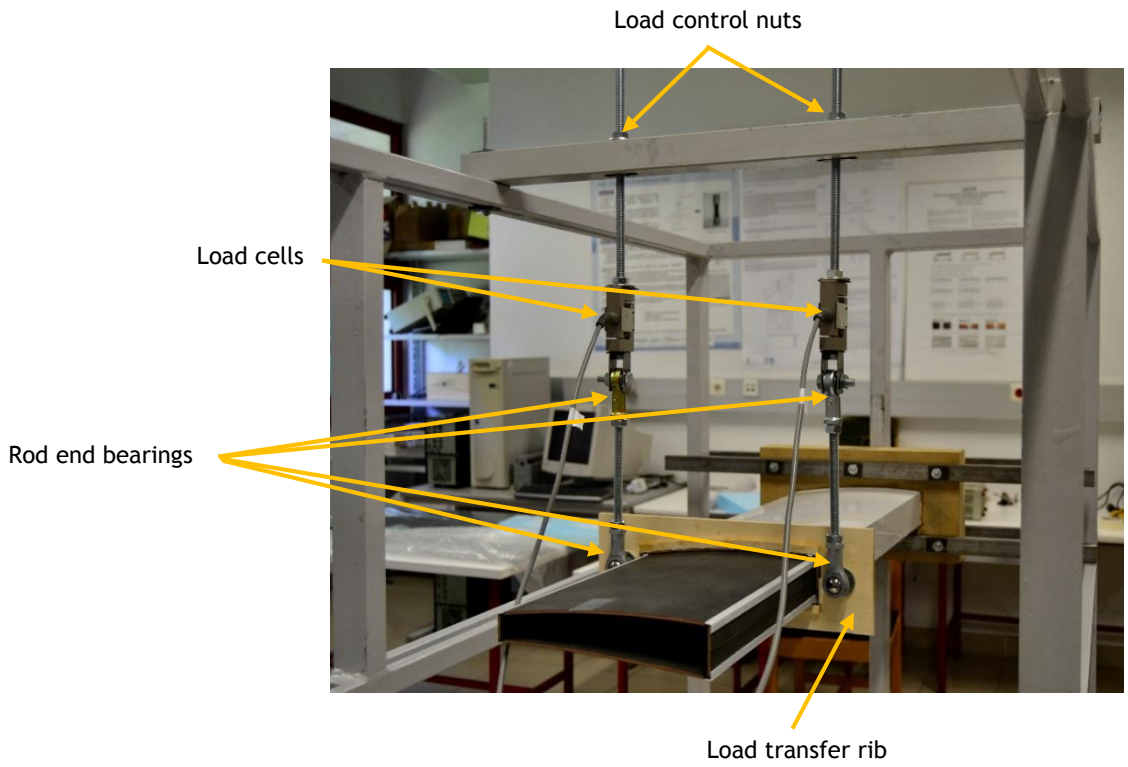

Figure 5.7: Jig's main components

5.2.1. Shear and bending moment diagrams

To build the shear and bending moment diagrams, a polynomial approximation of the ARA's curve slopes was made in order to obtain *k*, the lift distribution as a function of the position along the wing's semi-span (*y*). Then, lift, drag, pitching moment, horizontal force and vertical force were calculated by integration of the polynomial along the wing's semi-span. As the wing-box has been settled for 30 % and 70 % of the wing's chord, the vertical force was divided into two equivalent forces applied at those positions referred earlier being the subscripts 1 and 2 the force at 30 % of the wing's chord and the force at 70 % of the wing's chord, respectively. Figure 5.8 shows the distributed forces and its positions.

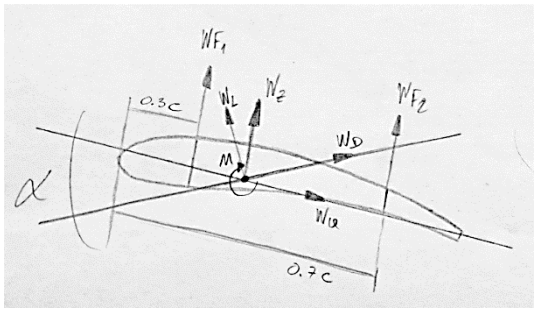

Figure 5.8: Distributed forces representation

The previous force distributions are given by the next equations.

$$wF_1\,(y) = wZl - \frac{-wT - 0.05\,wZl\,c_{ref}}{0.4\,c_{ref}} \tag{5.1}$$

Where:

wZl = k coeff(i) cos(a)

$$k = \frac{L}{\int_{-b/2}^{b/2} f(y)\,dy}$$

f(y) is a 5th order polynomial

coeff(i) = coefficients given by the polynomial approximation of ARA's curve slopes

a = angle of attack

wt = pitching moment distribution

c_{ref} = wing chord

$$wF_2\,(y) = \frac{-wT - 0.05\,wZl\,c_{ref}}{0.4\,c_{ref}} \tag{5.2}$$

Where:

wZl, wT and c_{ref} are referred to in equation (3.7)

For load factors of 1.5 to 4, Figure 5.9 shows the corresponding fore and aft forces distributions along the wing's semi-span.

Figure 5.10 shows the shear force diagram for load factors of 1.5 to 3.5, calculated from the analytical integration of the curves for wF_1 and wF_2 curves from Equations (3.7) and (3.8), respectively. Figure 5.11 shows the corresponding bending moment diagram for load factors of 1.5 to 3.5, calculated from the analytical integration curve of the shear force.

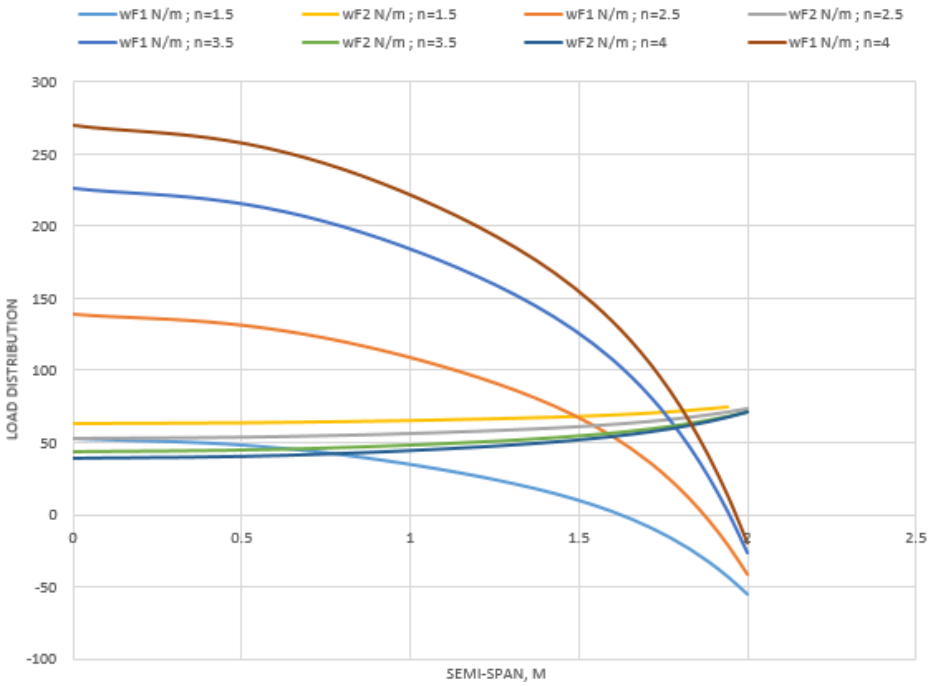

Figure 5.9: Lift and Drag distributions along the wing's semi-span

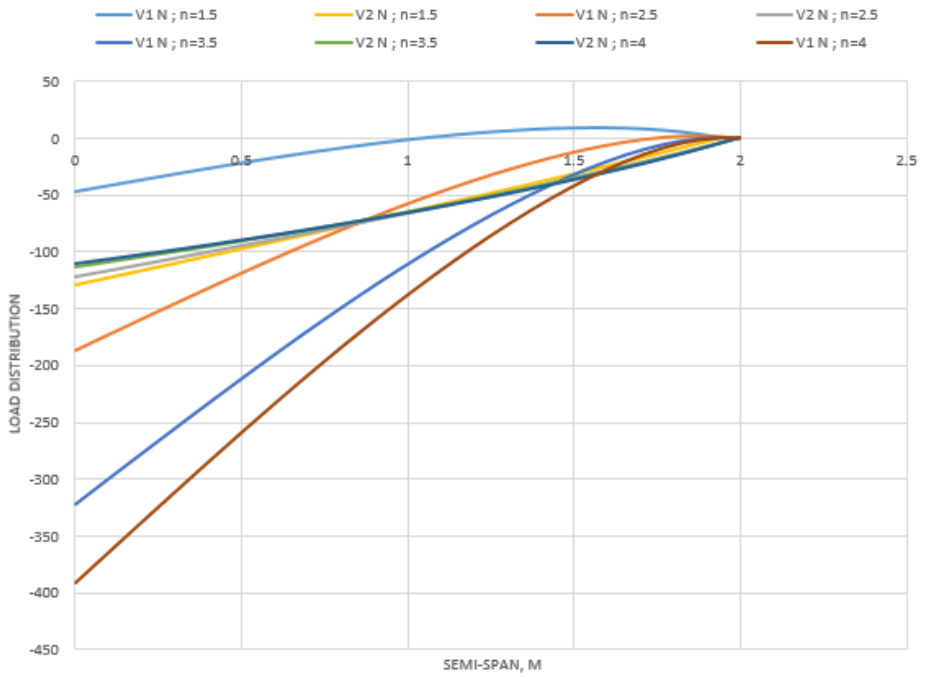

Figure 5.10: Shear diagram

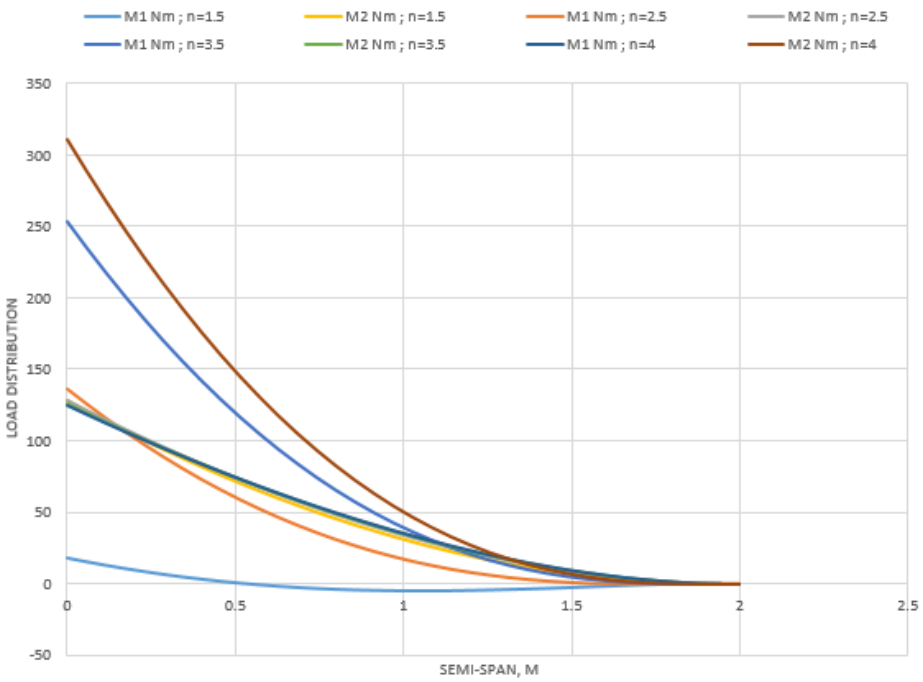

Figure 5.11: Bending moment diagram

5.3. Results

The values of the bending moment at the wing root were recalculated for the position in which they were applied at the wing-box at the experimental test. Table 5.1 resumes the loads applied at each position. Subscripts 1 and 2 denote the fore and aft loads, respectively.

Table 5.1: Experimental tests' fore and aft loads

Load Factor	Strain_1 [N]	Strain_2 [N]
1.5	50	132
2.5	186	116
3.5	323	101

Figure 5.12 demonstrates the values collected with the experimental tests representing the maximum deflection according to different load factors for fore and aft loads. For a load factor of 4.5 experimental tests were not made for safety reasons such as damaging the wing's prototype.

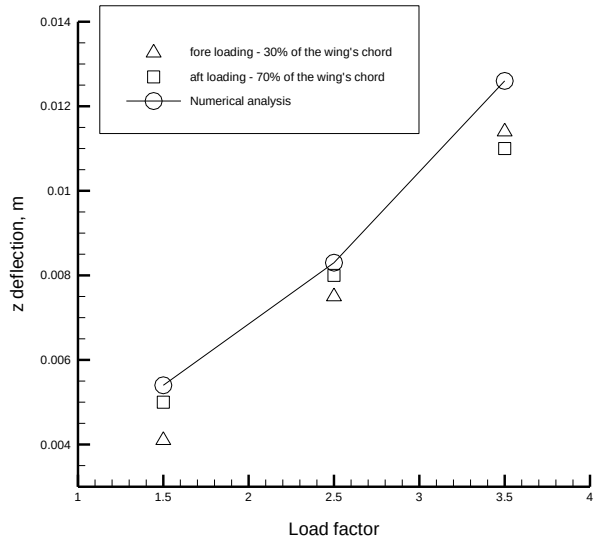

Figure 5.12: Experimental tests' results

Regarding the experimental tests' results, it was expected that the deflection increased, for the fore and rear loading, with increasing load factors. It is possible to see, from the shear force and bending moment diagrams, that the fore and aft loadings increase with increasing load factors and, as expected, this is reflected on the corresponding variation in the displacements.

Comparing the numerical model's results with the prototype experimental tests' results, the values are in good agreement. From Figure 5.12, for a semi-span of 2 m, it can be observed that, for a moving fraction of 0.25 and a load factor of 3.5, the displacement at a position of 0.608 m from the wing root, which is where the loads were applied at the experimental prototype, is around 0.0114 m. When compared to the numerical model, the values are close, being around 0.0126 m. Analysing the case for load factors of 1.5 and 2.5, the numerical model's displacements are around 0.005 m and 0.008 m, respectively, while in the experimental tests displacements of 0.0041 m and 0.0075 m were registered for load factors of 1.5 and 2.5, respectively.

6. Conclusions

6.1. Summary

In the past 20 years, many research groups worldwide have been attracted by shape morphing aircraft. Although interesting concepts have been presented, few have progressed to fabrication and testing and even fewer have had a flight test. Wing morphing is a promising technology because it allows the aerodynamic potential of an aircraft wing to be explored, by adapting the wing shape for several flight conditions encountered in a typical mission profile.

The UAVs are the technology of choice for many routine applications such as border patrol, environmental monitoring, meteorology, military operations, and research and rescue. This was possible with the exponential growth of satellite services. For these reasons and the lower productions costs, lower safety and certification requirements, and lower aerodynamic loads the focus on investigations on wing morphing is on UAVs. This allows great opportunity for small research groups to develop new technologies and attract industry attention. However it seems that the manufacturers are not 100 % reliant of the benefits to adopt morphing technologies in the near future, as many developed concepts have a technology readiness level that is still too low. [2]

With the development of smart materials and the advances made at this field new concepts on variable-geometry small aircraft have been developed. Usually, any morphing wing has to overcome the weight penalty that the actuation mechanisms impose. Compared to bigger and faster aircrafts, UAVs require more dramatic geometry changes so the aerodynamic properties become useful and perceptible.

Although the computational analysis is important for the development of any technology, experimentation and construction of prototypes remains imperative for larger companies. But with the development of algorithms and Computational Structural tools (using FEM), companies with fewer resources opt for this cheaper alternative.

With this work I was able to gain and deepen knowledge and accomplish the proposed objectives.

6.2. Numerical analysis

As expected from the parametric study, a 2 m wing with higher moving fraction is heavier than a wing with lower moving fraction. The reason behind this is the increased volume of material used to fabricate the OMW because the interface between the two portions of the wing also increases as its length is equal to the actual moving portion plus 0.15 m at an inner part to guarantee good functioning of the telescopic wing. It was also noticed that the maximum displacement (0.056 m) at the wing tip occurs for a wing with a moving fraction of 0.3 and the minimum displacement (0.033 m) occurs for a fraction of 0.175. For a moving fraction of 0.05,

a displacement of 0.042 m was registered. The collected values show that the moving fraction optimal value, for a semi-span of 2 m, is 0.175. The Failure Criteria, which is not higher than 0.57 for all cases, including the semi-spans of 2.5 m and 3 m reveals that the wing-box is oversized and tolerates the stresses which it is subjected to. Regarding the maximum twist angle, which appears at the wing tip, it is always less than 1 degree which indicates that the wing-box has the required torsional stiffness.

The values of the maximum deflection for a 2.5 m and a 3 m semi-span wings are similar and depict an almost equal polynomial fitting but, obviously, with slightly increased values for the 3 m semi-span.

During this part of the project the main difficulties were the following:

- Understanding the numerical model to make the necessary changes to it and manipulate it to obtain the desired results;
- Working with programming tools to obtain the polynomial equations that represent the mass and displacement variations according to the wing's moving fraction and its semi-span.

6.3. Experimental tests

The experimental tests are in good agreement with the numerical model. It can be said that the deflections obtained with the numerical model are slightly higher than the deflections measured from the experimental tests. The validity of the numerical model was confirmed and it can be concluded that wing-box prototype exhibits the predicted stiffness.

6.4. Suggestions for future work

Considering that the numerical model used does not contain the actuation mechanism coupled to the wing's structure it would be interesting to compare the collected data of the mass and deflection of the model used with a new numerical model.

To validate the parametric study new prototypes could be made with different mobile fractions.

7. References

[1] T. M. Young and M. Hirst, *Innovation in Aeronautics*. Elsevier, 2012, pp. 132–154.

[2] S. Barbarino, O. Bilgen, R. M. Ajaj, M. I. Friswell, and D. J. Inman, "A Review of Morphing Aircraft," *J. Intell. Mater. Syst. Struct.*, vol. 22, no. 9, pp. 823–877, Aug. 2011.

[3] M. Abdulrahim and R. Lind, "Using Avian Morphology to Enhance Aircraft Manoevrability," in *Proceedings of AIAA Atmospheric Flight Mechanics Conference and Exhibit*, 2006, pp. 21–24.

[4] T. A. Weisshaar, "Morphing Aircraft Technology - New Shapes for Aircraft Design," vol. RTO-MP-AVT, 2006.

[5] F. E. Culick, "The Wright Brothers: First Aeronautical Engineers and Test Pilots," *AIAA J.*, vol. 44, pp. 985–1006, 2003.

[6] S. P. Joshi, Z. Tidwell, W. A. Crossley, and S. Ramakrishnan, "Comparison of Morphing Wing Strategies Based Upon Aircraft Performance Impacts," in *Proceedings of the 45th AIAA/ASME/ASCE/AHS/ASC Structures, Structural Dynamics & Materials Conference*, 2004, p. 1722.

[7] J. Bowman, B. Sanders, B. Cannon, J. Kudva, S. Joshi, and T. A. Weisshaar, "Development of Next Generation Morphing Aircraft Structure," in *48th AIAA/ASME/ASCE/AHS/ASC Structures, Structural Dynamics and Materials Conference*, 2007, p. 1730.

[8] V. P. Galantai, "Design and Analysis of Morphing Wing for Unmanned Aerial Vehicles by Design and Analysis of Morphing Wing for Unmanned Aerial Vehicles," 2010.

[9] J. J. Anderson, *Fundamentals of Aerodynamics*, 3rd editio. Maryland: McGraw Hill Higher Education, 2011.

[10] J. N. Kudva and A. Jha, "Morphing Aircraft Concepts, Classifications and Challenges," in *Proceedings of SPIE smart Structures and Materials 2004: Industrial and Commercial Aplications of Smart Structure Technologies*, 2004, p. 5388.

[11] P. Bettini, A. Airoldi, G. Sala, L. Di Landro, M. Ruzzene, and A. Spadoni, "Composite chiral structures for morphing airfoils: Numerical analyses and development of a manufacturing process," *Compos. Part B Eng.*, vol. 41, no. 2, pp. 133–147, Mar. 2010.

[12] R. Vos and R. Barrett, "<title>Pressure adaptive honeycomb: a new adaptive structure for aerospace applications</title>," vol. 7647, p. 76472B–76472B–12, Mar. 2010.

[13] Edwards, "Inflatable Wings Given a Flutter," *Space Daily*, 2001. [Online]. Available: http://www.spacedaily.com/news/plane-inflatable-wing-01a.html.

[14] J. M. Rowe, S. W. Smith, A. Simpson, J. Jacob, and S. Scarborough, "Development of a Finite Element Model of Warping Inflatable Wings," in *AIAA/ASME/ASCE/AHS/ASC Structures, Structural Dynamics and Materials Conference*, 2006, pp. 1277–1294.

[15] A. Simpson, N. Coulombe, J. Jacob, and S. Smith, "Morphing of Inflatable Wings," 2005.

[16] CHANGE, "The CHANGE Project," 2012. [Online]. Available: http://change.tekever.com/.

[17] Smartbird, "Festo," 2011.

[18] A. J. Colozza, "Solid State Aircraft - Phase II Final Report Prepared for NASA Institute for Advanced Concepts," 2005.

[19] a. Y. N. Sofla, S. a. Meguid, K. T. Tan, and W. K. Yeo, "Shape morphing of aircraft wing: Status and challenges," *Mater. Des.*, vol. 31, no. 3, pp. 1284–1292, Mar. 2010.

[20] R. Ajaj, A. Keane, and D. Inman, "Morphing Aircraft : The Need for a New Design Philosophy," no. September, pp. 1–7, 2013.

[21] J. R. Blondeau and Pines, "Design, Development and Testing of a Morphing Aspect Ratio Wing Using Inflatable Telescopic Spar," in *Proceedings of 44th AIAA/ASME/ASCE/AHS/ASC Structures, Structural Dynamics, and Materials Conference*, 2003, p. 1718.

[22] J. E. Blondeau and D. J. Pines, "Pneumatic Morphing Aspect Ratio Wing," no. April, pp. 1–12, 2004.

[23] H. P. Monnera, M. Sinapiusa, and M. Kintschera, “DLR’s morphing wing activities within the European network,” in *Monnera, H. P., Sinapiusa, M., & Kintschera, M. (2014). DLR’s morphing wing activities within the European network. 23rd International Congress of Theoretical and Applied Mechanics*, 2014, p. 10: 364–375.

[24] “DARPA’s Morphing Program,” 2014. [Online]. Available: http://www.canosoarus.com/05UMAAV/UMAAV01.htm.

[25] L. Arrison, “2002-2003 AE / ME Morphing Wing Design,” 2003.

[26] R. D. Vocke, C. S. Kothera, B. K. S. Woods, E. A. Bubert, and N. M. Wereley, “Dimensional Morphing Structures for Advanced Aircraft, Recent Advances in Aircraft Technology,” *Ramesh K. Agarwal*, vol. ISBN: 978-, 2012.

[27] R. M. Ajaj, E. I. Saavedra Flores, M. I. Friswell, G. Allegri, B. K. S. Woods, a. T. Isikveren, and W. G. Dettmer, “The Zigzag wingbox for a span morphing wing,” *Aerosp. Sci. Technol.*, vol. 28, no. 1, pp. 364–375, Jul. 2013.

[28] M. Stern and C. Eli, “VAST AUAV (Variable AirSpeed Telescoping Additive Unmanned Air Vehicle),” 2013. [Online]. Available: http://api.ning.com/files/4zDRwQPj*wtaRefSFB0n6VcxLe5EPT4Qsylq2Ly19*COGCfLcZMqjebGcwfuoJMNugVdOKhKXlC1cdUpp2YHDzvjLHXhU*Xu/rapidPresentation.pdf.

[29] J. Felício, P. Santos, P. Gamboa, and M. Silvestre, “Evaluation of a Variable-Span Morphing Wing for a Small,” no. April, pp. 1–17, 2011.

[30] D. Alemayehu, R. Mcnulty, C. De Tenorio, and V. Tech, “Virginia Tech Morphing Wing Team Spring 2005 Final Report,” 2005.

[31] G. Warwhick, “NextGen’s shape changing UAV morphs in flight,” 2007. [Online]. Available: http://www.flightglobal.com.

[32] J. Vale, “Development of Computational and Experimental Models for the Synthesis of Span and Camber Morphing Aircraft Technologies. PhD Thesis,” Instituto Superior Técnico, 2012.

[33] P. Gamboa, J. Vale, F. J. P. Lau, and a. Suleman, “Optimization of a Morphing Wing Based on Coupled Aerodynamic and Structural Constraints,” *AIAA J.*, vol. 47, no. 9, pp. 2087–2104, Sep. 2009.

[34] P. de Marmier and N. Wereley, “Control of Sweep Using Pneumatic Actuators to Morph Wings of Small Scale UAVs,” in *44th Structures, Structural Dynamics and Materials Conference*, 2003, vol. American I.

[35] D. A. N. Iii, D. J. Inman, and C. Woolsey, “Design , Development , and Analysis of a Morphing Aircraft Model for Wind Tunnel Experimentation by Design , Development , and Analysis of a Morphing Aircraft Model for Wind Tunnel Experimentation,” 2006.

[36] F. Mattioni, A. Gatto, P. M. Weaver, and M. Friswell, “The application of residual stress tailoring of snap-through composites for variable sweep wings,” in *47th AIAA/ASME/ASCE/AHS/ASC Structures, Structural Dynamics, and Materials Conference*, 2006.

[37] M. D. Skillen and W. A. Crossley, “Modeling and Optimization for Morphing Wing Concept Generation II Part I: Morphing Wing Modeling and Structural Sizing Techniques. NASA Report,” pp. NASA/CR–2008–214902, 2008.

[38] K. Subbarao, A. H. Supekar, and K. Lawrence, “Investigation of Morphable Wing Structures for Unmanned Aerial Vehicle Performance Augmentation,” no. April, pp. 1–14, 2009.

[39] P. D. R. Santos, P. V Gamboa, P. M. B. Santos, and J. M. A. Silva, 23-27 June 2013 “Structural design of a composite variable-span wing,” in *Integrity, Reliability and Failure of Mechanical Systems, 4th International Conference on Integrity, Reliability and Failure*, vol. 1, pp. 1–12.

[40] P. V Gamboa, P. D. R. Santos, J. M. A. Silva, and P. M. B. Santos, 23-27 June 2013 “Flutter analysis of a composite variable-span wing,” in *Integrity, Reliability and Failure of Mechanical Systems, 4th International Conference on Integrity, Reliability and Failure*, vol. 1, pp. 1–14.

[41] EASA, “EASA’s Certification Specifications,” 2014. [Online]. Available: http://www.easa.europa.eu/document-library/certification-specifications?search=cs-23&date_filter[min][date]=&date_filter[max][date]=.

[42] Datasheet, “Models 615 and 616 Tension Compression Load Cells,” 2012. [Online]. Available: http://www.vishaypg.com/docs/12066/615-616.pdf.

[43] “NI PXIe-4330/4331 User Manual,” *Instruments, National*, 2014. [Online]. Available: http://www.ni.com/pdf/manuals/373029a.pdf.

[44] “FB-M12 12mm Right Hand Rod End Bearing,” *Rod end bearings*, 2014. [Online]. Available: http://www.bearingboys.co.uk/FB-M12_12mm_Right_Hand_Rod_End_Bearing-88488-p.

[45] “FB-M12S 12mm Studded Right Hand Rod End Bearing,” *Studded rod end bearings*, 2014. [Online]. Available: http://www.bearingboys.co.uk/FB-M12S_12mm_Studded_Right_Hand_Rod_End_Bearing_-88643-p.

8. Appendix

A.1

1903	1931	1931	1932	1937	1947	1951
						
Wright Flyer	Pterodactyl IV	MAK-10	IS-1	LIG-7	MAK-123	X 5
Twist	*Sweep*	*Span*	*Bi-to monoplane*	*Chord*	*Span*	*Sweep*
1952	1964	1964	1966	1967	1967	1969
		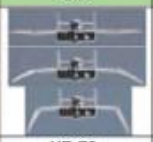				
XF10F	F 111	XB 70	Su 17 IG	MIG 23	SU 24	Tu 22 M
Sweep	*Sweep*	*Span bending*	*Sweep*	*Sweep*	*Sweep*	*Sweep*
1970	1972	1974	1974	1979	1981	1985
						
F 14	FS 29	B 1	Tornado	AD 1	Tu 160	AFTI/F 111
Sweep	*Span*	*Sweep*	*Sweep*	*Obliquing*	*Sweep*	*M.A.W.*
1993	1994	2001	2002	2003	2004	2005
						
FLYRT	MOTHRA	AAL	F/A 18	Virginia Tech	Univ. of Florida	Univ. of Florida
Span	*Camber*	*Pitch*	*A.A.W.*	*Span*	*Twist*	*Gull*
2006	2006	2007	2007	2007	2008	2010
			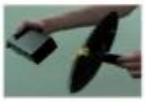			
MFX 1	Univ. of Florida	Virginia Tech	Univ. of Florida	MFX 2	Delft Univ.	Virignia tech
Sweep & Span	*Sweep*	*Camber*	*Folding*	*Sweep & span*	*Sweep*	*Camber*

Figure 8.1: Timeline of fixed wing aircraft implementing morphing technologies [2]

A.2)

Table A.1: Values collected from the wing-box structural analysis for Case A)

Semi-span [m]	Moving fraction [%]	Mass [Kg]	Displacement [m]	Wing twist [°]	Failure Criteria
	0,050	1,0770	0,041592	0,043782	0,311319
	0,075	1,0857	0,039365	0,045416	0,319381
	0,100	1,0945	0,037168	0,047117	0,327882
	0,125	1,1032	0,035032	0,048474	0,335566
	0,150	1,1120	0,033087	0,050015	0,340837
2,00	0,175	1,1207	0,032885	0,053777	0,346499
	0,200	1,1295	0,033836	0,059955	0,346700
	0,225	1,1382	0,036223	0,064460	0,344114
	0,250	1,1470	0,040456	0,070100	0,340466
	0,275	1,1558	0,046909	0,074943	0,333254
	0,300	1,1645	0,056024	0,080302	0,335451
	0,050	1,3277	0,072407	0,056791	0,391214
	0,075	1,3387	0,068112	0,059251	0,404444
	0,100	1,3496	0,063884	0,061517	0,419011
	0,125	1,3606	0,059914	0,064246	0,429605
	0,150	1,3715	0,056481	0,067872	0,439566
2,50	0,175	1,3824	0,055958	0,075053	0,447262
	0,200	1,3934	0,057324	0,083218	0,451611
	0,225	1,4043	0,061823	0,091186	0,455713
	0,250	1,4153	0,069530	0,097956	0,453328
	0,275	1,4262	0,081141	0,105124	0,446194
	0,300	1,4372	0,097730	0,110956	0,434761
	0,050	1,5785	0,112181	0,067683	0,465051
	0,075	1,5916	0,105238	0,071155	0,484970
	0,100	1,6048	0,099036	0,074984	0,506039
	0,125	1,6179	0,092448	0,078561	0,522566
	0,150	1,6310	0,086895	0,081641	0,536295
3,00	0,175	1,6442	0,086515	0,093456	0,548414
	0,200	1,6573	0,088523	0,102865	0,557658
	0,225	1,6704	0,096252	0,113402	0,563308
	0,250	1,6836	0,108363	0,123163	0,565334
	0,275	1,6967	0,127961	0,132613	0,559432
	0,300	1,7098	0,154924	0,142973	0,563751

Table A.2: Values collected from the wing-box structural analysis for Case B)

Semi-span [m]	Moving fraction [%]	Mass [Kg]	Displacement [m]	Wing twist [°]	Failure Criteria
	0,050	1,0195	0,04398	0,04905	0,31131
	0,075	1,0315	0,04177	0,04773	0,30738
	0,100	1,0434	0,03954	0,04591	0,31653
	0,125	1,0553	0,03733	0,04668	0,32011
	0,150	1,0673	0,03517	0,04844	0,32508
2,00	0,175	1,0792	0,03439	0,05270	0,32769
	0,200	1,0912	0,03515	0,05782	0,32811
	0,225	1,1031	0,03738	0,06294	0,32712
	0,250	1,1151	0,04143	0,06827	0,32144
	0,275	1,1270	0,04785	0,07285	0,31469
	0,300	1,1390	0,05689	0,07781	0,32386
	0,050	1,2559	0,075858	0,059471	0,391886
	0,075	1,2708	0,071672	0,058502	0,397381
	0,100	1,2858	0,067184	0,059397	0,405562
	0,125	1,3007	0,063250	0,061880	0,418201
	0,150	1,3156	0,058958	0,067405	0,423279
2,50	0,175	1,3306	0,058174	0,073367	0,433039
	0,200	1,3455	0,059464	0,080755	0,434662
	0,225	1,3605	0,063743	0,087795	0,434805
	0,250	1,3754	0,071206	0,094256	0,429678
	0,275	1,3903	0,082435	0,100918	0,425595
	0,300	1,4053	0,098514	0,106552	0,418169
	0,050	1,4923	0,117887	0,066840	0,465008
	0,075	1,5102	0,110790	0,069932	0,475768
	0,100	1,5282	0,103680	0,072780	0,495457
	0,125	1,5461	0,096796	0,076093	0,507644
	0,150	1,5640	0,090793	0,082899	0,520609
3,00	0,175	1,5819	0,089562	0,090677	0,535795
	0,200	1,5998	0,091409	0,100325	0,539560
	0,225	1,6178	0,097403	0,109953	0,538126
	0,250	1,6357	0,110838	0,117801	0,541964
	0,275	1,6536	0,128873	0,128337	0,541677
	0,300	1,6715	0,157762	0,133887	0,533002

Table A.3: Values collected from the wing-box structural analysis for Case C)

Semi-span [m]	Moving fraction [%]	Mass [Kg]	Displacement [m]	Wing twist [°]	Failure Criteria
	0,050	1,0035	0,04389	0,05509	0,30447
	0,075	1,0164	0,04166	0,05335	0,30267
	0,100	1,0292	0,03936	0,05092	0,30830
	0,125	1,0420	0,03720	0,04860	0,31512
	0,150	1,0538	0,03506	0,04834	0,32036
2,00	0,175	1,0677	0,03430	0,05251	0,32352
	0,200	1,0805	0,03508	0,05728	0,32497
	0,225	1,0934	0,03722	0,06308	0,32480
	0,250	1,1062	0,04121	0,06746	0,31977
	0,275	1,1190	0,04778	0,07230	0,31332
	0,300	1,1319	0,05681	0,07639	0,32073
	0,050	1,2360	0,075759	0,067241	0,382949
	0,075	1,2520	0,071358	0,065701	0,386798
	0,100	1,2681	0,067206	0,064838	0,401729
	0,125	1,2841	0,063128	0,062199	0,413374
	0,150	1,3001	0,059204	0,066483	0,422811
2,50	0,175	1,3162	0,058056	0,072862	0,426416
	0,200	1,3322	0,059450	0,079910	0,431598
	0,225	1,3483	0,063547	0,086128	0,431964
	0,250	1,3643	0,070968	0,092650	0,428654
	0,275	1,3803	0,082589	0,098119	0,422074
	0,300	1,3964	0,099231	0,102689	0,411394
	0,050	1,4684	0,117626	0,074233	0,455002
	0,075	1,4876	0,110760	0,074178	0,472159
	0,100	1,5069	0,102978	0,073504	0,484198
	0,125	1,5261	0,096327	0,077553	0,504202
	0,150	1,5454	0,090432	0,082340	0,517665
3,00	0,175	1,5646	0,088927	0,091851	0,527235
	0,200	1,5839	0,090363	0,100965	0,535489
	0,225	1,6031	0,098241	0,107811	0,540842
	0,250	1,6224	0,110558	0,115860	0,541802
	0,275	1,6416	0,129672	0,124437	0,538797
	0,300	1,6609	0,156517	0,133393	0,539871